J. Fluid Mech. (1993), *vol.* 246, *pp.* 267–299

Direct numerical simulation of transition to turbulence in Görtler flow

By WEI LIU AND J. ANDRZEJ DOMARADZKI
Department of Aerospace Engineering, University of Southern California, Los Angeles, CA 90089-1191, USA

(Received 8 January 1992 and in revised form 19 June 1992)

Using direct numerical simulation techniques we investigate transition to turbulence in a boundary-layer flow containing two large-scale counter-rotating vortices with axes aligned in the streamwise direction. The vortices are assumed to have been generated by the Görtler instability mechanism operating in boundary-layer flows over concave walls. Full, three-dimensional Navier–Stokes equations in a natural curvilinear coordinate system for a flow over concave wall are solved by a pseudospectral numerical method. The simulations are initialized with the most unstable mode of the linear stability theory for this flow with its amplitude taken from the experimental measurements of Swearingen & Blackwelder (1987). The evolution of the Görtler vortices for two different spanwise wavenumbers has been investigated. In all cases the development of strong inflexional velocity profiles is observed in both spanwise and vertical directions. The instabilities of these velocity profiles are identified as a primary mechanism of the transition process. The results indicate that the spanwise shear plays a more prominent role in the transition to turbulence than the vertical shear, in agreement with the hypothesis originally proposed by Swearingen & Blackwelder (1987). The following features of the transition, consistent with this hypothesis, were observed. Instability oscillations start in the spanwise direction and are followed later by oscillations in the vertical direction. A two-dimensional linear stability analysis predicts that the maximum growth rates of perturbations associated with the spanwise profiles are greater than those associated with the vertical profiles. Regions of high perturbation velocity correlate well with the regions of high spanwise shear and no obvious correlation with the vertical shear regions is observed. Finally, the analysis of the kinetic energy balance equation reveals that most of the perturbation energy production in the initial stages of transition occurs in the region characterized by large spanwise shear created by the action of the vortices moving low-speed fluid away from the wall. Our results are consistent qualitatively and quantitatively with other experimental, theoretical, and numerical investigations of this flow.

1. Introduction

Counter-rotating streamwise vortices are observed in transitional and turbulent boundary layers and seem to play an important role in transition to turbulence and in the dynamics of fully turbulent boundary layer flows (Blackwelder 1983). For this reason understanding their dynamics is considered very important for the development of practical techniques to control such flows. However, there is considerable disagreement concerning their origin, structure, and evolution. Good reviews of the present status of research on this subject and existing controversies are

given by Kline & Robinson (1989) and Robinson (1991). At least part of the difficulty in investigating streamwise vortices in turbulent boundary-layer flows is related to the fact that the mechanisms by which they are generated are largely unknown and in turbulent flows they occur randomly in space and time. For these reasons even the task of distinguishing them from the random turbulent background may be quite difficult. These difficulties led a number of researchers to consider simpler 'model' flows, which capture essential features of characteristic structures thought to dominate the dynamics of the turbulent boundary layers but which, by virtue of their deterministic generation mechanisms, are not contaminated by the turbulent background. A good example of such an approach are studies of hairpin vortices in laminar boundary layers performed by Acarlar & Smith (1987*a*, *b*).

In laminar boundary-layer flow over a concave wall, under proper conditions, streamwise vortices will develop due to the imbalance between the centrifugal forces and the radial pressure gradient as first predicted by Görtler (1940). The Görtler vortices share many similarities with vortical structures found in other types of boundary layers as documented by Blackwelder (1983). Since their generation mechanism through the instability process is known and they form a deterministic, spatially regular pattern, they may be considered as another example of a 'model' flow which can offer an attractive alternative in investigations of the dynamics of counter-rotating vortices in boundary layers.

Apart from a general interest in Görtler flow as a 'model' flow it is of interest on its own merit since the Görtler instability and a subsequent transition to turbulence are common phenomena in various flows involving curved boundaries, for instance flows over turbine blades. Görtler flow has been studied by many researchers since Görtler first discussed it in 1940. An extensive review of this subject given recently by Floryan (1991) contains almost 170 references. Most of the earlier theoretical research (Görtler 1940; Hämmerlin 1955; Smith 1955; and Floryan & Saric 1979) was concentrated on the linear stability theory of this flow and determining a neutral stability curve. A review of earlier results on this subject was given by Herbert (1976). The major difficulty associated with these works was a lack of the agreement among the neutral stability curves derived by different investigators. This disagreement was resolved only fairly recently by Hall (1982, 1983) who showed that a unique neutral curve does not exist for Görtler flow because its stability strongly depends on how and where the boundary layer is perturbed. Hall also pointed out that the parallel-flow assumption made in the stability analyses preceding his work was not correct, except in the small-spanwise-wavelength limit.

Experimental studies of Görtler flow were concentrated for the most part not on the emergence of the vortices caused by the primary instability of the laminar Blasius boundary layer but on the investigation of the evolution of the flow with the vortices already present. This is evident from the summary of experimental data of several investigators by Swearingen & Blackwelder (1987) who compared the data with the theoretical stability curves of both Floryan & Saric (1979) and Hall (1983). Most of the experimental points fall into the region which is unstable according to both theories. One of the first experimental investigations of Görtler flow was undertaken by Liepmann (1945) and its goal was to determine the conditions for its transition to turbulence. It is probably fair to state that this is still the principal goal of research in this area. The first stage in the transition process are deformations of the boundary-layer velocity profile by the vortices. Such deformations are well documented in the experiments of Tani (1962), Wortmann (1969), Tani & Aihara (1969), Bippes (1972), Winoto & Crane (1980), and Swearingen & Blackwelder (1987).

At this initial stage of transition the flow is steady and when visualized in the plane parallel to the wall using a smoke-wire technique it is characterized by the accumulation of smoke between the vortices where the measured streamwise velocity is lower than in the surroundings (e.g. Swearingen & Blackwelder 1987). This low-speed region is located where the vortices induce the maximum vertical flow away from the wall, the upwash region. When the flow is visualized in the plane normal to the wall and to the flow direction it exhibits a characteristic structure of a 'mushroom' (Peerhossaini & Wesfried 1988) with smoke concentrated between the vortices forming the 'mushroom's' stem and its hat formed by smoke spread in the upper parts of the boundary layer by the vortical flow turning to the sides. Subsequent evolution of the flow involves spanwise oscillations of low-speed streaks clearly visible in planes parallel to the wall (Bippes 1972; Swearingen & Blackwelder 1987) as well as in planes normal to the wall (Peerhossaini & Wesfried 1988). At this stage of transition Swearingen & Blackwelder (1987) observed that the spanwise oscillations are often accompanied by the appearance of horseshoe vortices forming over the low-speed streaks. After a distance equal to several streamwise wavelengths of the spatial waviness associated with the oscillations, flow becomes turbulent.

The appearance of the waviness and the horseshoe vortices in the experiments is usually attributed to secondary instabilities of the boundary-layer flow modified by the action of the vortices. Several theoretical investigations of these instabilities were undertaken recently. The secondary instability of Görtler flow presents a formidable mathematical problem since the base flow has three non-vanishing components of the velocity which all depend on both spanwise and normal-to-the-wall coordinates, and may also depend weakly on the streamwise coordinate if the boundary-layer growth is taken into account. For this reason various simplifications of the problem are introduced. Since the secondary instability wavelength observed experimentally is on the order of the boundary-layer thickness non-parallel effects are usually neglected in the analysis. After the dependence on the streamwise coordinate is eliminated the various analyses of this problem differ mostly in the form of the assumed base flow. Park & Huerre (1992) performed a secondary instability analysis of the Görtler flow in a boundary layer with an asymptotic suction velocity profile which is parallel by definition. The base flow was obtained from temporal two-dimensional numerical simulations. Yu & Liu (1991) also investigated the stability of the flow obtained in two-dimensional simulations of the Görtler vortices evolving in the Blasius boundary layer. These simulations, performed by Sabry & Liu (1988, 1991), assumed a temporally growing boundary layer and the correspondence between time in the simulations and the locations in the spatially growing boundary layer in experiments was established using a convection velocity. To our knowledge, Hall & Horseman (1991) are the only ones who used as a base flow results of nonlinear evolution of Görtler flow in a spatially growing boundary layer (Hall 1988). All these investigations identify two distinct modes of the secondary instability: a sinuous mode for the perturbation pattern which is antisymmetric about the low-speed region, and a varicose mode for the pattern which is symmetric about the low-speed region. These are also the instability modes observed in the experiments.

In the above secondary instability investigations the base flow is generated by performing numerical simulations of the perturbed laminar boundary layer. In the simulations of Hall (1983, 1988) the perturbation is introduced at some location in the boundary layer and is advanced in the streamwise direction using the system of time-independent partial linear parabolic equations, which are derived from the full Navier–Stokes equations, until the Görtler flow with the appropriate strength

develops. In simulations of Park & Huerre (1992) and Sabry & Liu (1988, 1991) the boundary layer is assumed to be parallel and it is perturbed by the Görtler vortex system obtained from the linear stability analysis. Subsequently, two-dimensional Navier–Stokes equations are advanced in time until the evolved flow shows characteristic features of the Görtler flow observed in experiments. Both approaches reproduce qualitatively, and in many instances also quantitatively, the experimental evolution of the Görtler flow in the steady flow regime, where the simplifications of the Navier–Stokes equations made are justified. For instance, all these simulations predict generation of the inflexional profiles of the streamwise velocity, development of the low-speed streaks and 'mushroom' structures in planes normal to the wall, etc. However, such simulations cannot be extended into the transitional regime, in which the flow is both unsteady and three-dimensional.

In this work we report the results of the direct numerical simulations of full three-dimensional Navier–Stokes equations for Görtler flow experiencing transition to turbulence. The direct numerical simulation technique is thus extended to a regime which was previously investigated using only experimental and theoretical methods and we expect that our results will provide a useful database complementing those obtained using different approaches. The purpose of our work is to develop an efficient numerical code capable of modelling three-dimensional boundary-layer flows over concave walls and to investigate the physics of such flows, in particular the mechanisms of transition to turbulence. One of the main goals is to assess the relative importance to the transition process of the inflexional profiles of the streamwise velocity in the normal and the spanwise direction. Classical (and casual) explanations of this process in bounded flows containing counter-rotating vortices attribute it to shear-layer instabilities occurring on the inflexional profiles normal to the wall induced by the vortices. Thus it came as a surprise when Swearingen & Blackwelder (1987) reported that in the transition process the *spanwise* inflexional profiles of the streamwise velocity may be more pronounced than the normal profiles and may be responsible for triggering the transition. If the spanwise shears also play an important role in the fully turbulent flows this fact may require significant changes in the classical Reynolds decomposition used in describing turbulent boundary layers. This is because the classical description assumes that the boundary layer is statistically homogeneous in the spanwise direction and thus eliminates the turbulent energy production mechanism by the spanwise shears. The transitional and weakly turbulent Görtler flow is a useful model which allows the testing of various methods of description of the wall-bounded flows containing streamwise vortices and will be used here for this purpose.

2. The numerical method

2.1. *Basic equations*

The vorticity form of the Navier–Stokes equations for incompressible flow is

$$\partial \boldsymbol{u}/\partial t = \boldsymbol{u} \times \boldsymbol{\omega} - \boldsymbol{\nabla} \Pi/\rho + \nu \nabla^2 \boldsymbol{u}, \tag{1}$$

$$\boldsymbol{\nabla} \cdot \boldsymbol{u} = 0, \tag{2}$$

where $\boldsymbol{u}$ is the velocity, $\boldsymbol{\omega} = \boldsymbol{\nabla} \times \boldsymbol{u}$ is the vorticity, ρ is the density, $\Pi = p + \frac{1}{2}\rho \boldsymbol{u}^2$ is the pressure head, and ν is the kinematic viscosity.

Equations (1) and (2) are transformed into a natural curvilinear coordinate system for the flow over a curved boundary with radius of curvature R. The system of

coordinates is chosen such that x is the ordinate along the curved boundary, z is the ordinate in the direction normal to the boundary, and y is in the spanwise direction. Equations (1) and (2) have the following form in this curvilinear coordinate system:

$$\frac{\partial}{\partial t} = v\left(\frac{1}{h}\partial_x v - \partial_y u\right) - w\left(\partial_z u - \frac{1}{h}\partial_x w - \frac{\kappa}{h}u\right) + \nu\left[\frac{1}{h^2}\partial_x^2 u + \partial_y^2 u + \partial_z^2 u - \frac{\kappa}{h}\partial_z u - \frac{2\kappa}{h^2}\partial_x w - \frac{\kappa^2}{h^2}u\right] - \frac{1}{\rho}\frac{1}{h}\partial_x \Pi, \quad (3)$$

$$\frac{\partial}{\partial t}v = w(\partial_y w - \partial_z v) - u\left(\frac{1}{h}\partial_x v - \partial_y u\right) + \nu\left[\frac{1}{h^2}\partial_x^2 v + \partial_y^2 v + \partial_z^2 v - \frac{\kappa}{h}\partial_z v\right] - \frac{1}{\rho}\partial_y \Pi, \quad (4)$$

$$\frac{\partial}{\partial t}w = u\left(\partial_z u - \frac{1}{h}\partial_x w - \frac{\kappa}{h}u\right) - v(\partial_y w - \partial_z w) + \nu\left[\frac{1}{h^2}\partial_x^2 w + \partial_y^2 w + \partial_z^2 w - \frac{\kappa}{h}\partial_z w + \frac{2\kappa}{h^2}\partial_x u - \frac{\kappa^2}{h^2}w\right] - \frac{1}{\rho}\partial_z \Pi, \quad (5)$$

$$\frac{1}{h}\partial_x u + \partial_y v + \partial_z w - \frac{\kappa}{h}w = 0, \quad (6)$$

where $(u, v, w) = \boldsymbol{u}$, $\kappa = 1/R$ is the curvature of the boundary, $h = 1 - \kappa z$, and derivatives with respect to x, y, and z are denoted by ∂_x, ∂_y, and ∂_z, respectively.

2.2. *Computational procedure*

Equations (3)–(6) are solved using a modified version of the semi-implicit, pseudospectral numerical code FLOGUN developed originally by Orszag & Kells (1980) for the simulation of channel flows. A detailed review of pseudospectral techniques used in computational fluid mechanics is given by Gottlieb, Hussaini & Orszag (1984) and Canuto *et al.* (1988).

The numerical code employs the fractional step method after regrouping equations (3)–(6) as follows:

$$\frac{\partial}{\partial t}u = \left\{v\left(\frac{1}{h}\partial_x v - \partial_y u\right) - w\left(\partial_z u - \frac{1}{h}\partial_x w - \frac{\kappa}{h}u\right) - \nu\kappa\left(\frac{2}{h^2}\partial_x w + \left(\frac{1}{h} - 1\right)\partial_z u\right)\right\} + \left\{\nu\left(\frac{1}{h^2} - 1\right)\partial_x^2 u - \nu\frac{\kappa^2}{h^2}u\right\} + \{\nu[\partial_x^2 u + \partial_y^2 u + \partial_z^2 u - \kappa\partial_z u]\} - \left\{\frac{1}{\rho}\frac{1}{h}\partial_x \Pi\right\}, \quad (7)$$

$$\frac{\partial}{\partial t}v = \left\{w(\partial_y w - \partial_z v) - u\left(\frac{1}{h}\partial_x v - \partial_y u\right) - \nu\kappa\left(\frac{1}{h} - 1\right)\partial_z v\right\} + \left\{\nu\left(\frac{1}{h^2} - 1\right)\partial_x^2 v\right\} + \{\nu[\partial_x^2 v + \partial_y^2 v + \partial_z^2 v - \kappa\partial_z v]\} - \left\{\frac{1}{\rho}\partial_y \Pi\right\}, \quad (8)$$

$$\frac{\partial}{\partial t}w = \left\{u\left(\partial_z u - \frac{1}{h}\partial_x w - \frac{\kappa}{h}u\right) - v(\partial_y w - \partial_z v) - \nu\kappa\left(-\frac{2}{h^2}\partial_x u + \left(\frac{1}{h} - 1\right)\partial_z w\right)\right\} + \left\{\nu\left(\frac{1}{h^2} - 1\right)\partial_x^2 w - \nu\frac{\kappa^2}{h^2}w\right\} + \{\nu[\partial_x^2 w + \partial_y^2 w + \partial_z^2 w - \kappa\partial_z w]\} - \left\{\frac{1}{\rho}\partial_z \Pi\right\}, \quad (9)$$

$$\frac{1}{h}\partial_x u + \partial_y v + \partial_z w - \frac{\kappa}{h}w = 0. \quad (10)$$

The right-hand sides of (7)–(9) are written as sums of nonlinear, linear, viscous, and pressure terms (each within braces) which provide four differential operators used in the fractional step method, consisting of four separate steps. The last step involves solution of pressure and incompressibility equations, resulting in a divergence-free velocity field after a full sequence of the fractional steps is applied. The splitting errors were reduced using modified boundary conditions suggested by Fortin, Peyret & Temam (1971) and Zang & Hussaini (1986).

The form of (3)–(6) is affected by the curvature of the wall through the appearance of various terms and factors containing κ and $h(z) = 1-\kappa z$. For numerical stability reasons, the viscous term should be treated implicitly. However, the presence in the equations of the factor $h(z)$ dependent on the variable z prevents in this case the use of efficient methods developed for solutions of Poisson and Helmholtz equations in Cartesian coordinates. To circumvent this difficulty the viscous term is rewritten as in (7)–(9), resulting in a form which allows the application of the efficient numerical solvers at our disposal. The remaining portions of the original viscous term, which can be diagonalized in the spectral representation, form additional linear terms and those that cannot be diagonalized are included into the nonlinear terms.

We assume that the boundary layer is parallel, which allows the application of periodic boundary conditions in the horizontal directions. In these directions a spectral Fourier representation is used in the numerical method. Correspondingly, the collocation points in the physical space are equally spaced. In the vertical, non-periodic direction we use mapping from the channel flow to the boundary-layer flow geometry:

$$z^*(s) = \cos(\pi s), \quad -1 \leqslant s \leqslant 1, \tag{11}$$

$$z(s) = \tfrac{1}{2}b(1+z^*)/[a-\tfrac{1}{2}(1+z^*)]. \tag{12}$$

The mapping parameters are chosen as $a = 1.0225$ and $b = 14.0625$ which results in $0 \leqslant z \leqslant 93.75$, equivalent to about fifteen Blasius boundary-layer thicknesses, $\delta = 6.02$, in the non-dimensional units used here. The gridpoints in the vertical direction are Chebyshev collocation points obtained from (11) and (12) using uniform increments in the variable s. This allows efficient evaluation of z-derivatives using the Chebyshev collocation method.

Using Fourier expansions in the horizontal directions, the quantities in physical space and spectral space are related through the following relations:

$$q(x,y,z,t) = \sum_{|m|<M} \sum_{|n|<N} \hat{q}(k_x, k_y, z, t) \exp(ik_x x) \exp(ik_y y), \tag{13}$$

where $k_x = 2\pi m/L_x$, $k_y = 2\pi n/L_y$ are the horizontal wavenumbers, m and n are integers, and L_x and L_y give the size of the computational box. This mixed Fourier–physical space representation for the horizontal and vertical directions, respectively, is used as a primary representation for all dependent variables and the equations in the numerical program.

2.3. *Tests of the numerical code*

A standard test of such a numerical code is the comparison between the growth rates predicted by the code and the growth rates calculated from the linear stability theory. Following the original analysis of Görtler (1940) and Hämmerlin (1955) for parallel Görtler flow we introduce the velocity perturbations in the form

$$u = U_b(z) + u_1(z) \cos(\bar{\alpha} y)\, e^{\beta t}, \tag{14}$$

$$v = v_1(z) \sin(\bar{\alpha} y)\, e^{\beta t}, \tag{15}$$

$$w = w_1(z) \cos(\bar{\alpha} y)\, e^{\beta t}, \tag{16}$$

α	G	β_{LT}	β_{NS}	ϵ
0.300	2.40	+0.004800	+0.004779	+0.0044
0.300	1.60	+0.003660	+0.003634	+0.0071
0.300	0.80	+0.000739	+0.000701	+0.0510
0.300	0.30	−0.006794	−0.006874	+0.0120
0.200	1.00	+0.002089	+0.002056	+0.0160
0.243	5.12	+0.005557	+0.005541	+0.0029
0.276	6.00	+0.006131	+0.006116	+0.0024

TABLE 1. Comparison between growth rates of Görtler flow calculated from the linear stability theory and predicted by the Navier–Stokes solver

where $\bar{\alpha} = 2\pi/\lambda$ is a (dimensional) wavenumber in the spanwise direction and λ is a corresponding wavelength, β is the temporal growth rate, $U_b(z)$ is the mean flow, assumed here to be the Blasius profile, and $u_1(z)$, $v_1(z)$, and $w_1(z)$ are the perturbation amplitudes of the Görtler flow.

For parallel flow independent of the streamwise coordinate x the Navier–Stokes equations (3)–(6) simplify to

$$u_t + vu_y + w\left(u_z - \frac{1}{R-z}u\right) = \nu\left(u_{yy} + u_{zz} - \frac{1}{R-z}u_z\right), \tag{17}$$

$$v_t + vv_y + wv_z = -\frac{1}{\rho}p_y + \nu\left(v_{yy} + v_{zz} - \frac{1}{R-z}v_z\right), \tag{18}$$

$$w_t + vw_y + ww_z + \frac{u^2}{R-z} = -\frac{1}{\rho}p_z + \nu\left(w_{yy} + w_{zz} - \frac{1}{R-z}w_z\right), \tag{19}$$

$$v_y + w_z - \frac{1}{R-z}w = 0. \tag{20}$$

Substituting (14)–(16) into (17)–(20) and linearizing the equations leads to the following linear eigenvalue problem for the amplitudes $u_1(z)$, $v_1(z)$, and $w_1(z)$, which are the eigenfunctions, and the growth rate β, which is the corresponding eigenvalue:

$$\left(\frac{\mathrm{d}^2}{\mathrm{d}z^2} - \bar{\alpha}^2\right)u_1 - \frac{1}{\nu}\frac{\mathrm{d}U_b}{\mathrm{d}z}w_1 = \frac{\beta}{\nu}u_1, \tag{21}$$

$$\left(\frac{\mathrm{d}^2}{\mathrm{d}z^2} - \bar{\alpha}^2\right)^2 w_1 + \frac{2\bar{\alpha}^2}{\nu(R-z)} = \frac{\beta}{\nu}\left(\frac{\mathrm{d}^2}{\mathrm{d}z^2} - \bar{\alpha}^2\right)w_1, \tag{22}$$

$$v_1 = -\frac{1}{\bar{\alpha}}\frac{\mathrm{d}w_1}{\mathrm{d}z}. \tag{23}$$

This eigenvalue problem is solved using a standard solver provided by a mathematical library. The governing non-dimensional control parameter is Görtler number, $G = (U_0\theta/\nu)(\theta/R)^{\frac{1}{2}}$, where θ is the momentum thickness of the boundary layer and U_0 is the free-stream velocity. The growth rates β_{LT} calculated from the linear theory for different values of Görtler number and non-dimensional wavenumbers $\alpha = 2\pi/\lambda$ are compared in table 1 with the growth rates β_{NS} obtained from the full Navier–Stokes simulations initialized with the most unstable mode of the linear theory for a given G and α. Both sets of the results agree up to four figures after the decimal point with the relative error $\epsilon = (\beta_{NS} - \beta_{LT})/\beta_{LT}$ varying between 0.2% and 5%, with the largest relative errors for the smallest growth rates. The relative

errors in the growth rates obtained by Orszag & Kells (1980) using their numerical code to simulate Tollmien–Schlichting waves in plane Poiseuille flow and plane Couette flow are of the same order of magnitude as errors obtained here. An additional test of the code was made by initializing the three-dimensional velocity field with the velocity components v and w as random numbers with a Gaussian distribution and a small amplitude. The Görtler number was $G = 2.71$ and the non-dimensional wavenumber was $\alpha = 0.0664$, corresponding to the unstable state according to the linear theory. After about 500 time steps this initially random velocity perturbation began a process of self-organization which after additional 500 time steps resulted in a pattern of streamwise Görtler vortices. Thus the Görtler vortices are generated naturally by the numerical code.

3. Results of the numerical simulations

3.1. *Comparison with the experiments*

Two complete numerical simulations of a three-dimensional transition process in the Görtler flow were performed. For the comparison with the experimental results of Swearingen & Blackwelder (1987) we used values of the simulation parameters consistent with their experiment in which the radius of the wall curvature R was 3.2 m and the free streamwise velocity U_0 was 5 m/s. The initial condition in our simulations is a superposition of a Blasius mean flow and the most unstable mode of the linear stability theory for a parallel Görtler flow (see §2.3). The amplitude of the initial Görtler vortices, $0.167U_0$, and the initial Görtler number, 4.985, in the simulations are equal to the experimental values quoted by Swearingen & Blackwelder (1987) at the location $X_0 = 60$ cm from the leading edge. To simulate background noise present in the experiments a random velocity perturbation was added to the initial velocity field. The amplitude of the random component varied in z as $(z/\delta)^6 \exp(-(z/\delta)^2)$, consistent with the form of the velocity perturbation used by Hall (1983) in his stability analysis of Görtler flow. The maximum value of the amplitude, attained at $z = 0.76\delta$, was 0.5% of U_0. Our computational domain is a rectangular box. For one simulation, hereafter referred to as run A, the box has the size 2.2 cm in the x-direction, 2.3 cm in the y-direction, and 24.85 cm in the z-direction. For the other, hereafter referred to as run B, the box size is 2.0 cm in the x-direction, 1.8 cm in the y-direction, and 24.85 cm in the z-direction. Two values of the spanwise wavelength, 2.3 cm and 1.8 cm, were used; the former, run A, corresponding to the average spanwise wavelength observed in the experiments and the latter, run B, corresponding to the distance between two low-speed regions at the location where the detailed data were recorded in the experiments. The dimension of the computational box in the vertical direction was chosen to be much larger than the boundary-layer thickness but small enough to have an adequate spatial resolution in this direction with 129 mesh points used. The maximum value of the displacement thickness in the simulations was at most 1 cm so that the first condition is satisfied. The dimensions of the box in the streamwise direction x were chosen to accommodate one wavelength of the secondary instability mode observed in the experiments, usually between 2 and 2.5 cm. To maximize the numerical resolution with a finite number of mesh points we tended to choose values of this parameter from the lower end of the above range. The maximum resolution used in each horizontal direction was 64 collocation points.

Because of the parallel-mean-flow assumption the boundary layer in the simulations grows in time through viscous diffusion. In the experiments the

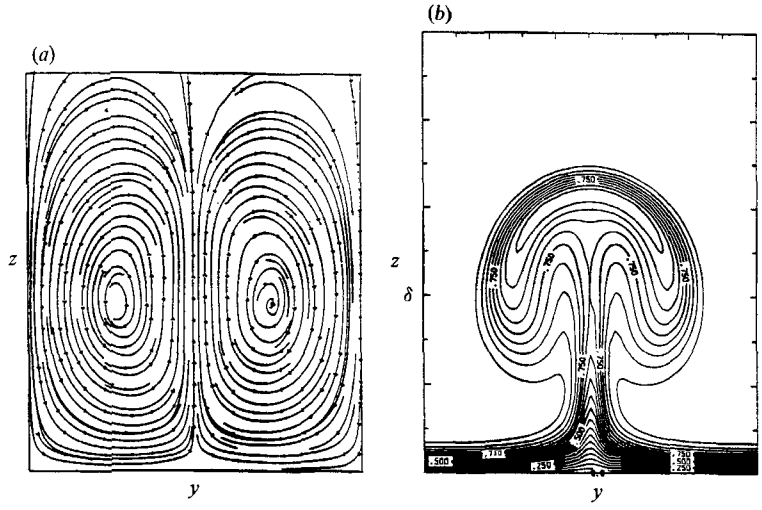

FIGURE 1. Structure of the velocity field in laminar Görtler flow. (*a*) Streamlines of the velocity in the (y,z)-plane (run A). (*b*) Iso-contours of the streamwise velocity u in the (y,z)-plane (run A).

boundary layer grows with increasing distance from the leading edge, also because of the action of viscosity. In order to compare the numerical results for the simulated time-evolving flow with the results obtained experimentally for the spatially evolving flow it is standard practice to introduce a convection velocity U_c which is used to convert temporal data into spatial ones. The convection velocities used in our work are $U_c = 0.60U_0$ and $U_c = 0.64U_0$ for run A and run B, respectively. These values of the convection velocities provide good agreement between both sets of data in the laminar two-dimensional regime but may be too large in the transitional and the turbulent regime. In what follows X denotes the distance of the computational box from the leading edge converted from the time in the simulations using the convection velocity U_c. The coordinate in the streamwise direction within the computational box is denoted by x.

There is no one-to-one correspondence between temporally evolving flows in the numerical simulations and spatially evolving flows in the experiments and comparisons between them must be made with caution. We cannot expect to reproduce exactly the experimental results in our simulations but we hope that the process of breakdown of streamwise vortices in wall-bounded flows has universal features which will be present in the experiments as well as in the simulations. Indeed, the secondary stability analyses performed with different assumptions about the detailed structure of the Görtler vortices and discussed in the Introduction all seem to provide very similar results concerning the transition. We may thus be justified in our expectations of identifying the important features of the transition process even without one-to-one correspondence between the simulations and the experiments.

The structure of the velocity field in the laminar regime $X = 40$–90 cm is shown in figure 1 (*a*) as a streamline plot in the plane normal to the wall and to the streamwise direction. The counter-rotating vortices pump fluid with a low streamwise velocity away from the wall creating the characteristic 'mushroom' structure of the iso-contour of the streamwise velocity shown in figure 1 (*b*) and reported by many other investigators. In this regime the flow is two-dimensional, with all quantities depending only on the normal and spanwise coordinates, but all three components of

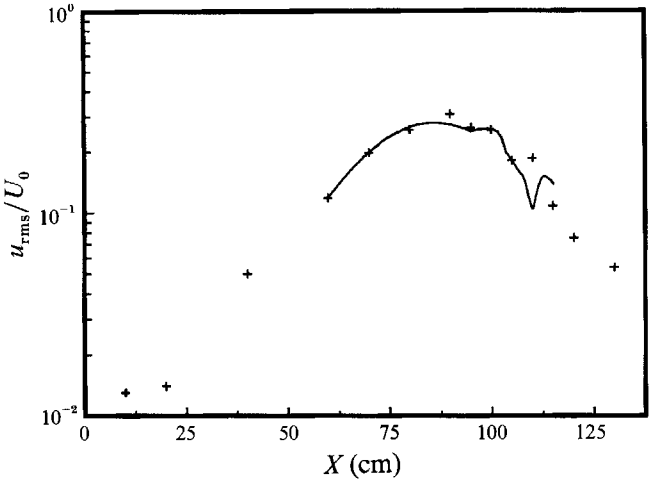

FIGURE 2. Streamwise evolution of the r.m.s. amplitude of the Görtler vortices U_G (run B): ——, computation; +, experiment.

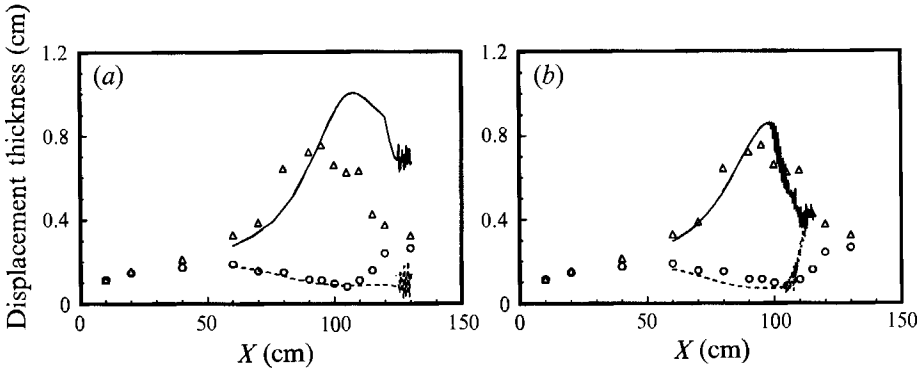

FIGURE 3. Streamwise evolution of the boundary-layer displacement thickness measured in the simulations at a selected (x, y) point in the peak region (solid curve) and in the valley region (broken curve), and corresponding experimental points from Swearingen & Blackwelder (1987) (△, peak; ○, valley): (*a*) run A, (*b*) run B.

the velocity are non-zero. The flow contains a low-speed region of streamwise velocity in the upwash region between the vortices and a high-speed region in the downwash region, in experiments referred to as a peak region and a valley region, respectively.

The r.m.s. value of the amplitude of the Görtler vortices in the simulations is defined as

$$U_G = \max_z \left(\frac{1}{L_y L_x} \int_0^{L_y} \int_0^{L_x} \left[u(x,y,z) - \frac{1}{L_y L_x} \int_0^{L_y} \int_0^{L_x} u(x,y,z)\,\mathrm{d}x\,\mathrm{d}y \right]^2 \mathrm{d}x\,\mathrm{d}y \right)^{\frac{1}{2}}, \quad (24)$$

and its streamwise evolution is shown in figure 2 for run B. A corresponding quantity measured in the experiments of Swearingen & Blackwelder (1987) was determined as the maximum r.m.s. amplitude of the spanwise variation of the u-component of the velocity for each downstream location X and is also plotted in figure 2. In view of the assumptions made to convert quantities from the simulations of the temporally evolving flow into quantities for the spatially evolving flow the comparison between both sets of data must be considered as very good.

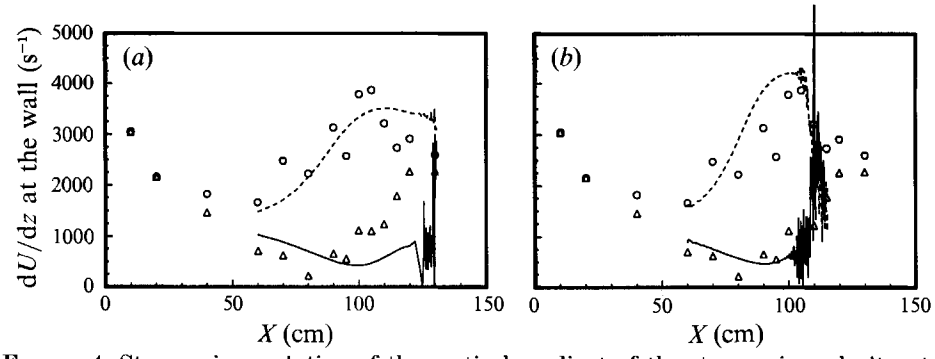

FIGURE 4. Streamwise evolution of the vertical gradient of the streamwise velocity at the wall measured in the simulations at a selected (x, y) point in the peak region (solid curve) and in the valley region (broken curve), and corresponding experimental points from Swearingen & Blackwelder (1987) (△, peak; ○, valley): (*a*) run A, (*b*) run B.

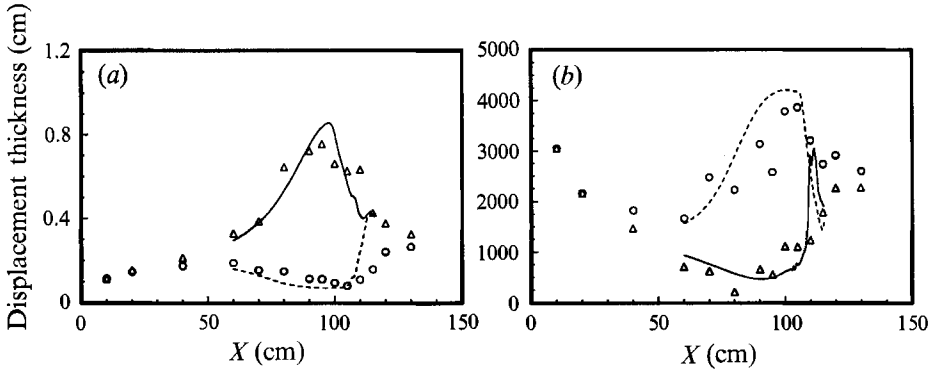

FIGURE 5. Streamwise evolution of the quantities averaged over lines in the x-direction within the computational box for run B (compare with figures 3 and 4): (*a*) boundary-layer displacement thickness, (*b*) vertical gradient of the streamwise velocity at the wall. Symbols as in figures 3 and 4.

The streamwise evolution of the boundary-layer displacement thickness and the evolution of the vertical gradient of the streamwise velocity, both recorded at two fixed (x, y) locations at the wall, one in the peak and the other in the valley region, are shown in figures 3 and 4, respectively, where they are compared with the experimental results of Swearingen & Blackwelder (1987). The displacement thickness grows in the low-speed region and decreases in the high-speed region as the flow develops in the streamwise direction. The displacement thickness may become greater by one order of magnitude in the low-speed region than in the high-speed region. For comparison, the Blasius boundary-layer thickness δ for a corresponding flow without vortices would be almost constant in the same range of streamwise locations X. More precisely, under the same conditions the Blasius boundary-layer thickness δ grows from 0.92 to 1.08 cm as X varies from 80 to 110 cm. In both runs at a distance about 90–100 cm from the leading edge, the displacement thickness in the low-speed region reaches its highest value and starts to decrease. The quantities computed as instantaneous values at the given wall locations show a large degree of variation toward the end of the runs. This indicates the beginning of transition to turbulence. The results of averaging these quantities in the x-direction within our computational box with y fixed in the peak and valley regions is shown in figure 5 for run B. At the end of the simulation such averaged quantities have almost the same values in both the low- and high-speed regions and the flow is weakly turbulent.

Comparison of figures 3(*a*) and 3(*b*) reveals that the flow transitions to turbulence at $X \approx 120$ cm in run A and at an earlier location, $X = 100$ cm, in run B. Also, the maximum value of the displacement thickness in the low-speed region reached in run A (1 cm), exceeds the maximum reached in run B (0.85 cm). After reaching the maximum the displacement thickness begins to decrease. In run B this decrease is associated with the appearance of unsteadiness and three-dimensional effects in the flow but in run A even after the displacement thickness curve begins to turn down at $X \approx 105$ cm the flow remains steady and two-dimensional until $X \approx 120$ cm. Interestingly, this effect of the turning down of the boundary-layer displacement thickness in the low-speed region is also predicted by purely two-dimensional simulations of the Görtler flow performed by Sabry & Liu (1988). These results indicate that the conventional explanations of this effect, ascribing it to the appearance of unsteadiness and three-dimensionality in the flow associated with the transition to turbulence cannot hold universally for all spanwise wavelengths of the vortices.

It seems that it may be possible to attribute this effect entirely to the existence of two-dimensional Görtler vortices. Near the leading edge the Görtler vortices pump vertically the low-speed fluid away from the wall in the peak region and push the high-speed fluid toward the wall in the valley region. Therefore the boundary-layer displacement thickness grows in the peak and decreases in the valley region. However, we may expect that after sufficiently long time the Görtler vortices will begin to transfer the high-speed fluid, which accumulates in the valley region, to the peak region by pushing it horizontally near the wall towards the convergence zone between the vortices. This will result in an increase of the streamwise velocity of the fluid near the wall in the peak region (see figure 7), and a corresponding decrease of the displacement thickness at this streamwise location X.

To support the above argument the following estimate of the location of the turning-down point can be made. Since the initial amplitude of the streamwise velocity of the Görtler vortices in the simulations is $0.167U_0$, and it increases almost linearly to $0.424U_0$ at the turning-down point, the average amplitude in this region is about $0.3U_0$. In laminar Görtler flow the amplitudes of spanwise and vertical velocities are one order of magnitude less than that of the streamwise velocity. Therefore an estimate of their amplitude is about $0.03U_0$. For the experimental value of the free-stream velocity $U_0 = 5$ m/s this last estimate provides the amplitude of the velocity V_G in the plane perpendicular to the streamwise direction of about 15 cm/s. The initial streamwise location in the simulations measured from the leading edge is $X_0 = 60$ cm, and the corresponding Blasius boundary-layer thickness δ is 0.8 cm. We estimate the distance l that the high-speed fluid from the outer parts of the boundary layer must travel to enter the low-speed region near the wall in the upwash region as the sum of δ and the half the spanwise wavelength, $\lambda_y = 0.9$ cm for run B, giving $l \approx 1.7$ cm. Thus the time needed for this process is to occur $t \approx l/V_G = 0.11$ s. Since the convection velocity U_c in the run B is $0.64U_0 = 320$ cm/s, the location of the point where the displacement thickness in the low-speed region will begin to decrease can be estimated as $X = X_0 + U_c t \approx 95$ cm, in fairly good agreement with the simulation results. We thus conclude that the observed initial growth and the subsequent decrease of the boundary-layer thickness in the peak region can be attributed to the action of the purely two-dimensional Görtler vortices.

The above discussion reveals that all qualitative features as well as many quantitative features of the flow observed in experiments are properly reproduced by the simulations.

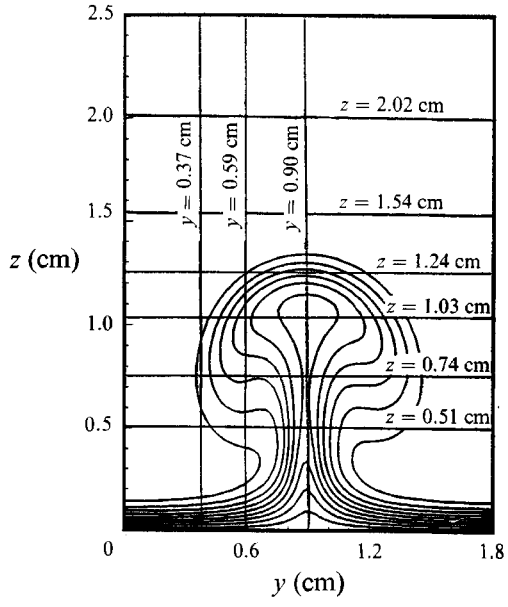

FIGURE 6. Iso-contours of the streamwise velocity u at the streamwise location $X = 98.3$ cm and the locations of planes and points where various physical quantities were recorded in run B.

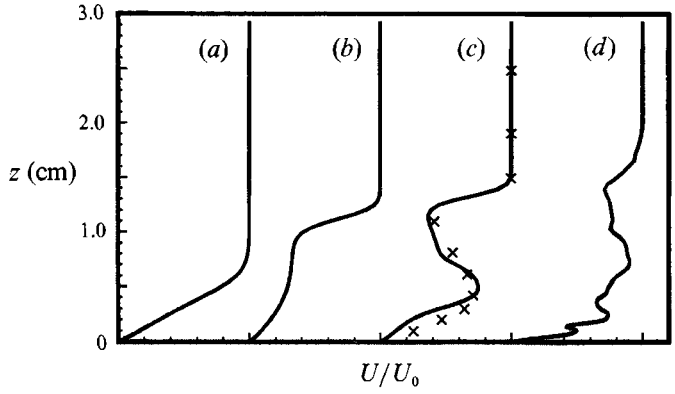

FIGURE 7. Profiles of the streamwise velocity in the vertical direction z in the low-speed region at different locations from the leading edge: (*a*) $X = 64$ cm, (*b*) 94 cm, (*c*) 100 cm, (*d*) 109 cm (run B). In (*c*) experimental results of Swearingen & Blackwelder (1987) and also plotted (×).

3.2. *The evolution of the streamwise velocity field*

Figure 6 shows iso-contours of the streamwise velocity u in the plane normal to the flow direction at the streamwise position $X = 98.3$ cm obtained in run B. Also, in this figure we have marked the locations of points and cuts where various physical quantities were recorded in the simulations and are plotted in this and in the following sections.

Profiles of the streamwise velocity in the vertical direction z taken in the low-speed region at different locations X from the leading edge are shown in figure 7. Also, for the location $X = 100$ cm the corresponding experimental results of Swearingen & Blackwelder are plotted in this figure. The pumping action of the counter-rotating vortices gradually generates an S-shaped profile with two inflexional points in the

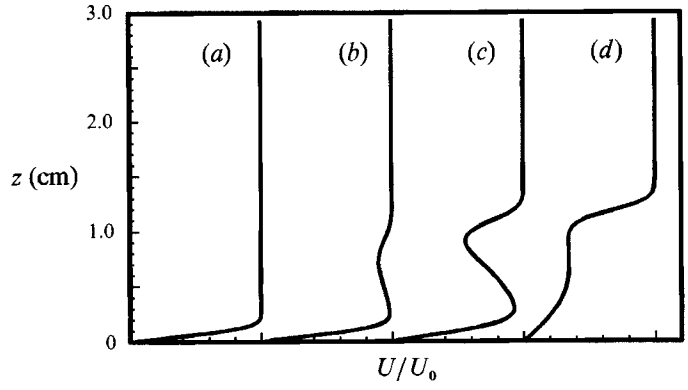

FIGURE 8. Profiles of the streamwise velocity in the vertical direction z at different spanwise locations y: (*a*) $y = 0.00$ cm, (*b*) 0.37 cm, (*c*) 0.59 cm, (*d*) 0.90 cm ($X = 96$ cm, run B).

regions of intense local horizontal shear layers. These regions move upwards and the associated shear strengths increase with increasing distance from the leading edge. The inflexional profiles in the vertical direction are observed not only in the low-speed region between the vortices, but in any vertical cut passing through the 'mushroom' region as seen in figure 8 which shows the velocity profiles at the same location X from the leading edge but different spanwise positions y. However, the vertical shear $\partial u/\partial z$ has its maximum in the low-speed region between the vortices. At the later stages of the flow evolution the appearance of turbulence decreases the intensity of these shear layers.

Streamwise velocity profiles in the spanwise direction y obtained by cutting the velocity field from run B at different z-locations are shown in figure 9. At $z = 1.54$ cm $\approx 1.5\delta$, where δ is the Blasius boundary-layer thickness, the streamwise velocity is essentially uniform and equal to the free-stream velocity U_0. As the wall is approached from above, the velocity profiles gradually change and become similar to two-dimensional wake profiles. The velocity deficit in the central peak region is caused by the Görtler vortices moving fluid with low streamwise velocity away from the wall. On the other hand, in the side valley regions the Görtler vortices push the high-speed fluid from the upper parts of the boundary layer towards the wall and in these regions the streamwise velocity is equal to the free-stream velocity U_0 for all z-locations of the spanwise cuts considered in figure 9. At larger distances X from the leading edge some of these plots exhibit local minima on either side of the central minimum. They are caused by the Görtler vortices which, after moving the low-speed fluid vertically from the wall, begin to move it to the sides and eventually begin to return it towards the wall. All these wake-like velocity profiles have inflexional points which are associated with the presence of the local, vertically oriented shear layers. In the initial stages of the simulations, the intensity of these shear layers intensifies with time. However, similarly to the case of the horizontal shear layers associated with the inflexional velocity profiles in the vertical direction, at the later stages of the evolution the intensity of the vertical shear layers is decreased by the appearance of turbulence.

The generation of such convolved streamwise velocity fields by the counter-rotating vortices in boundary layers was noted in almost all previous works on the subject and our results are no exception. However, it may be important to note that despite such a qualitative agreement between different investigations, the quantitative agreement not always is good. For instance, in calculations of Sabry & Liu

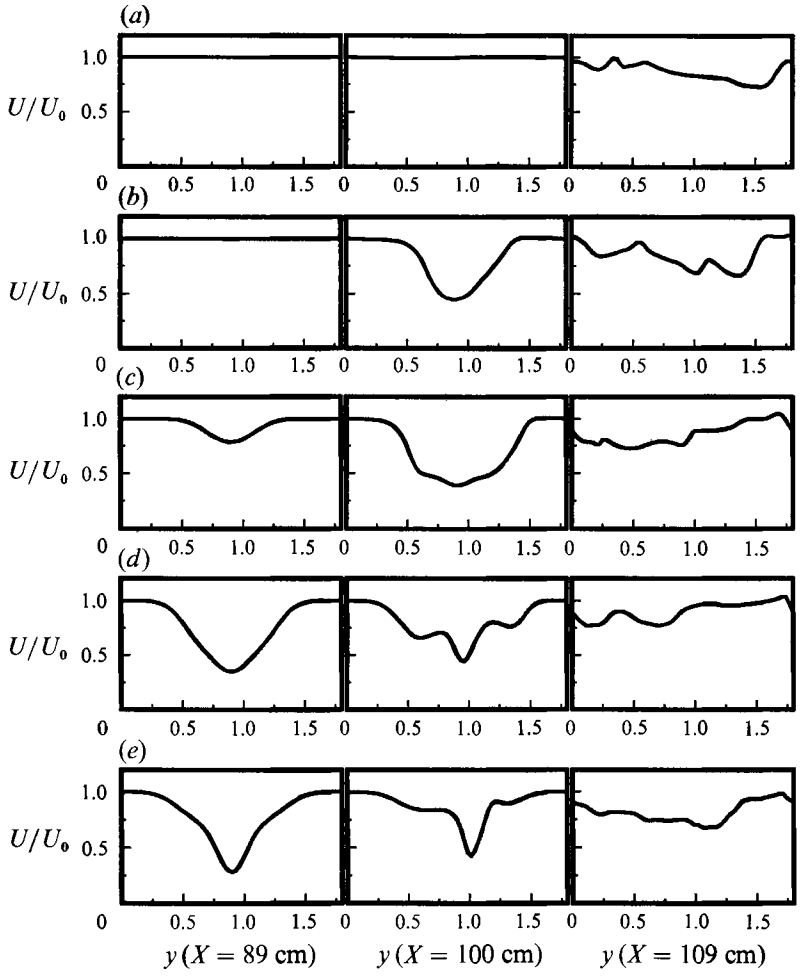

FIGURE 9. Profiles of the streamwise velocity in the spanwise direction y at three streamwise locations $X = 89$, 100, and 109 cm, and at different vertical locations z: (*a*) $z = 1.54$ cm, (*b*) 1.24 cm, (*c*) 1.03 cm, (*d*) 0.74 cm, (*e*) 0.51 cm (run B).

(1991) the velocity profile in the vertical direction in the low-speed region at $X =$ 100 cm is much less distorted than observed experimentally and in our simulations (figure 7). Such differences are probably caused by the assumptions underlying these investigations e.g. two-dimensional *vs.* three-dimensional formulation, use (or neglect) of initial random forcing, differences in the assumed convective velocities.

3.3. *Time series and stability analysis*

The time series of the spanwise and the vertical components of the velocity recorded at several points on a vertical line in the low-speed region in run B are shown in figures 10 and 11. The initial time $t = 0$ s in these figures corresponds to the streamwise location from the leading edge $X = 85.5$ cm. Initially, at all z-locations the spanwise velocity component v is zero. The vertical velocity component w is also constant, but not necessarily zero, since this is the upwash region. Near time $t \approx$ 0.03 s, corresponding to the location $X \approx 96$ cm from the leading edge, the oscillations in spanwise velocity records begin. The first oscillations in the vertical velocity records are observed at the later time, $t \approx 0.04$ s, corresponding to the location $X \approx$

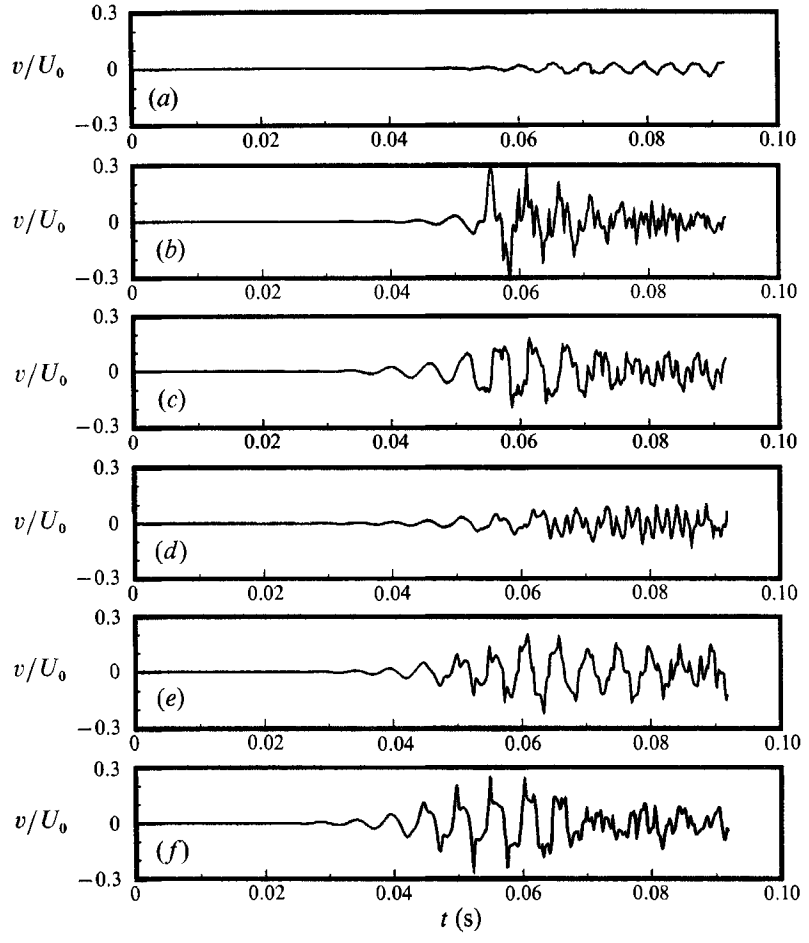

FIGURE 10. Time series of the spanwise velocity v in the low-speed region recorded at different vertical locations z: (*a*) $z = 2.02$ cm, (*b*) 1.54 cm, (*c*) 1.24 cm, (*d*) 1.03 cm, (*e*) 0.74 cm, (*f*) 0.51 cm ($y = 0.90$ cm, run B).

99 cm from the leading edge. In both cases, however, the oscillations are observed earlier at z-locations closer to the wall than at locations further away from the wall. For instance, in figure 10 we observe about 0.01 s delay, equivalent to a distance of more than 3 cm in the streamwise direction, between the start of the oscillations at $z = 0.51$ cm and at $z = 1.54$ cm. We therefore conclude that in this run the spanwise oscillations in the low-speed region start earlier than the vertical oscillations, and the oscillations in the inner region precede the oscillations in the outer regions of the boundary layer.

After the start of the oscillations their amplitude gradually increases and, in at least several plots, the observed time series pattern is fairly repeatable for a few oscillation periods. By counting numbers of peaks present in a given time interval in the time series with a distinct repeatable pattern we can get an estimate of the frequency of these oscillations. The observed frequency of the oscillations of the spanwise velocity component v is about 200 Hz and the observed frequency of the oscillations of the vertical velocity w is approximately twice as large, i.e. about 400 Hz. Similar time series of the vertical velocity were also taken at spanwise locations away from the low-speed region and are shown in figure 12. In

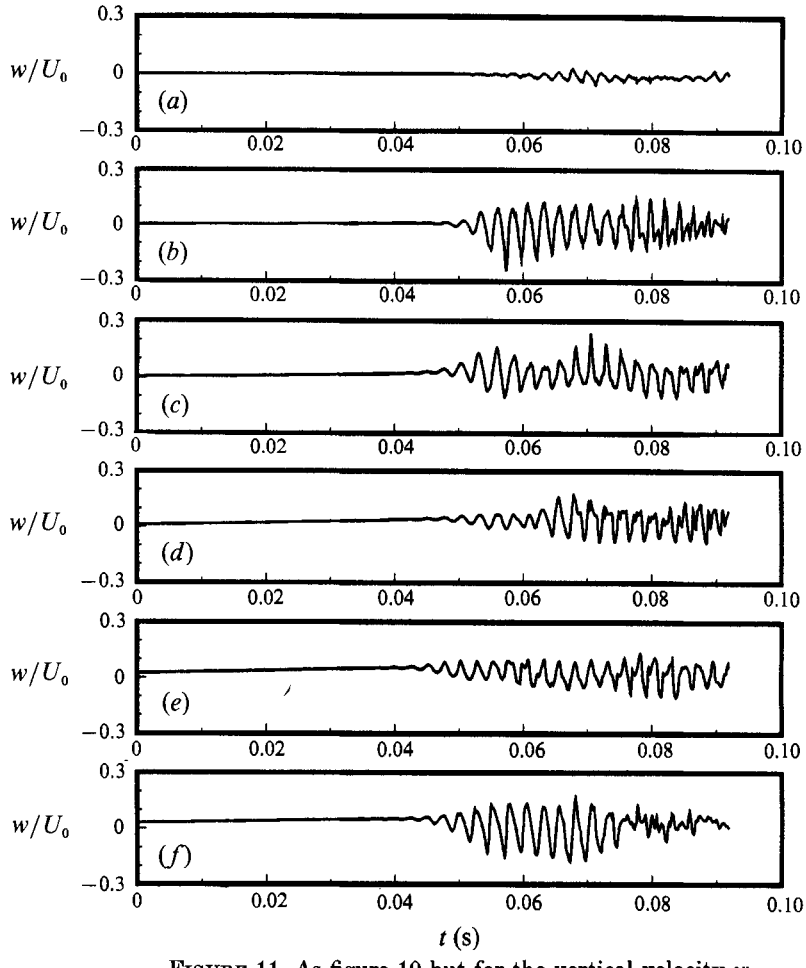

FIGURE 11. As figure 10 but for the vertical velocity w.

contradistinction to the previous case the frequency of the oscillations read from this figure is about 200 Hz and is the same as that for the spanwise velocity. The physical reasons for different frequencies of the vertical velocities observed in the low-speed region and away from it will be explained in §3.4.

The oscillations in the velocity traces for the transitional Görtler flow have also been reported in experiments of Bippes (1972) and Swearingen & Blackwelder (1987). In particular, the frequency of the oscillations in the outer region recorded by Swearingen & Blackwelder (1987) is about 130 Hz. Our numerical simulations do not predict this frequency. Possible reasons for this discrepancy will be given below.

In the last subsection we noted that the Görtler vortices interacting with the boundary-layer flow in the two-dimensional regime deform the surface $u(y, z)$ of the streamwise velocity such that the inflexional velocity profiles of the streamwise velocity u are observed in the one-dimensional cuts through this surface. In general, such a velocity field will be inviscidly unstable. Indeed, recent studies of the secondary instabilities of Görtler flow (Park & Huerre 1992; Yu & Liu 1991; Hall & Horseman 1991) properly identify main features of the transition observed in the experiments. Since the base flow in these stability analyses has three non-vanishing components of velocity, which all depend on two coordinates, y and z, the stability

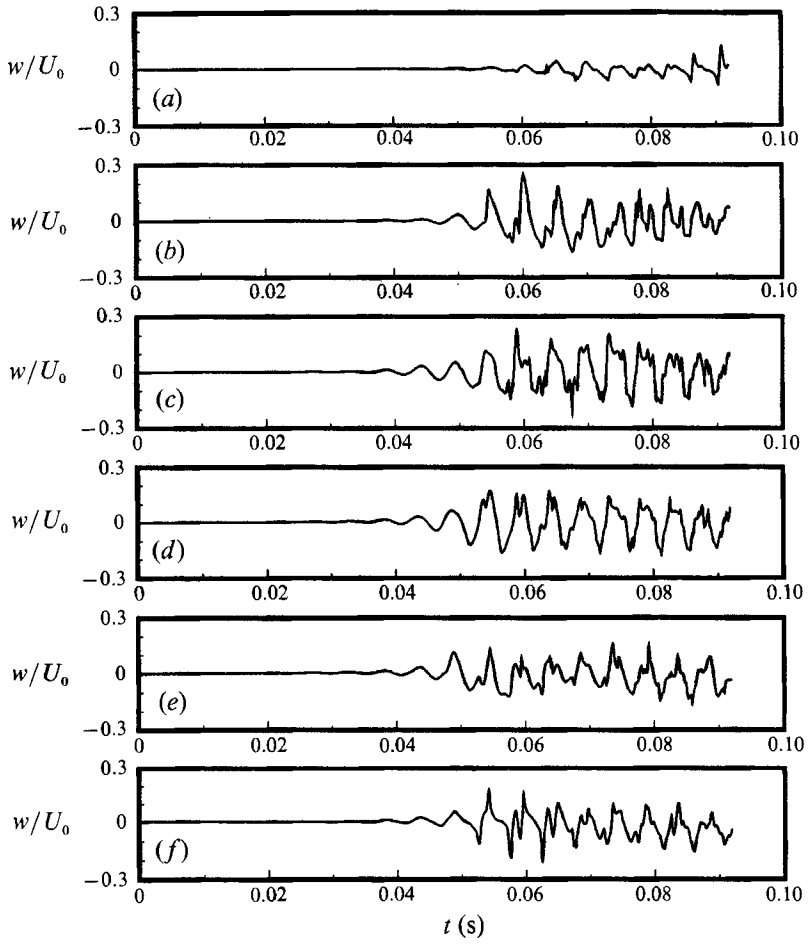

FIGURE 12. As figure 10 but for the vertical velocity w recorded away from the low-speed region ($y = 0.59$ cm).

analyses present a fairly complicated mathematical problem. A simpler approach, though more difficult to justify, is to investigate the stability of the one-dimensional streamwise velocity profiles obtained as cuts through the two-dimensional surface $u(y, z)$. Such an approach was used by Sabry, Yu & Liu (1990) with some success in predicting frequencies of the secondary instability oscillations that were in fair agreement with the experimental results of Swearingen & Blackwelder (1987).

Here, we apply this approach to the velocity fields obtained in the simulations. Our goals are, on one hand, to assess the applicability and the limitations of such a simplified stability analysis, and, on the other hand, to establish the viability of a postulated link between the observed process of transition and the instabilities of the inflexional velocity profiles. Direct numerical simulations are particularly useful in making such assessments. In direct numerical simulations both the transition process and the velocity profiles can be accurately documented and any relation between them can be established in a more self-consistent manner than in comparing theoretical results with experiments, where the assumed theoretical velocity profiles usually differ in some respects from the experimental ones. To proceed with the analysis we must assume that the timescale for the instabilities of the inflexional

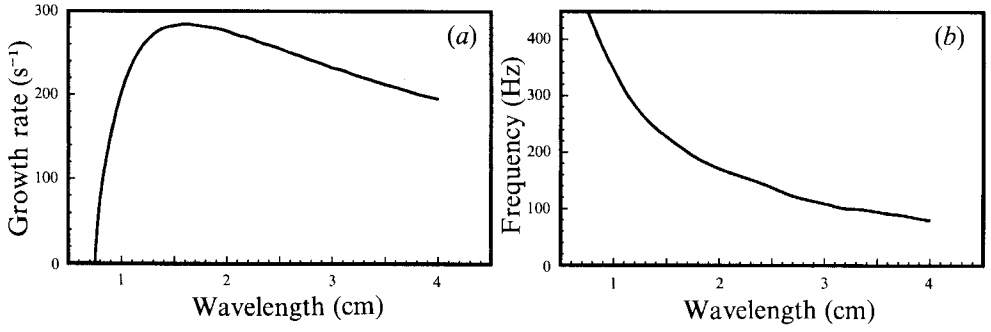

FIGURE 13. (*a*) A growth rate and (*b*) a frequency *vs.* wavelength calculated for a profile of the streamwise velocity in the vertical direction in the low-speed region ($X = 98$ cm, run B).

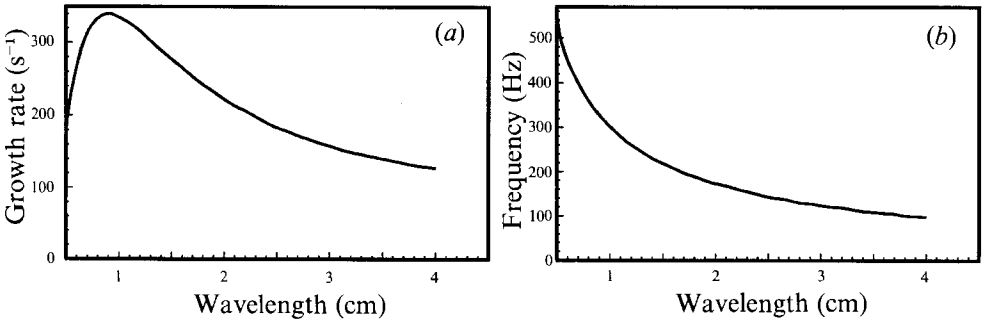

FIGURE 14. (*a*) A growth rate and (*b*) a frequency *vs.* wavelength calculated for a profile of the streamwise velocity in the spanwise direction at $z/\delta = 0.5$ where $\delta \approx 1$ cm ($X = 98$ cm, run B).

profiles is much smaller than that for the primary Görtler flow, i.e. the Görtler flow is assumed to be quasi-steady for the purpose of the stability analysis. This assumption will be subsequently confirmed by the results of the analysis. We performed a standard stability analysis employing the Orr–Sommerfeld equation applied to various steady one-dimensional vertical and spanwise velocity profiles obtained in the simulations. The Orr–Sommerfeld equation was solved with periodic boundary conditions for the spanwise profiles and homogeneous (zero) boundary conditions for the vertical profiles. In all reported cases the velocity profiles were determined from run B at distance $X = 98$ cm from the leading edge, just before transition begins.

Figure 13 shows a growth rate and a frequency of an unstable mode as a function of its streamwise wavelength, calculated for the streamwise velocity profile obtained from a cut in the vertical direction in the low-speed region. The same quantities are calculated for the velocity profile in the spanwise direction at $z/\delta = 0.5$ and are plotted in figure 14. The maximum growth rates for the vertical and spanwise profiles are 282 s^{-1} and 340 s^{-1}, respectively. The growth rate of the primary Görtler instability, calculated using the method of §2.3, is 20 s^{-1}. Therefore, the assumption of quasi-steady Görtler flow used in the analysis is applicable. The finite size of the computational domain in the streamwise direction imposes restrictions on allowable wavenumbers of the unstable modes. In the simulations only modes with wavelength equal to the size of the computational box in the x-direction (2.0 cm) were observed. For such a wavelength the frequencies of the oscillations predicted by this stability analysis for the velocities w and v are approximately 170 and 200 Hz, respectively.

These values are in good agreement with the fundamental frequency 200 Hz observed in the simulation, supporting the argument that the inviscid instabilities of inflexional velocity profiles of the streamwise velocity initiate the transition to turbulence in Görtler flow.

We were unable to observe in the simulations the frequency 130 Hz, which was observed in the experiment (Swearingen & Blackwelder 1987). Inspection of figures 13 and 14 reveals that the frequency 130 Hz is associated with the spanwise wavelength 2.5 cm. It therefore appears that we are unable to reproduce this frequency in our simulations because the streamwise size of the computational box is only 2.0 cm.

The most serious disagreement between the simulations and the above stability analysis is the fact that the instability mode observed in the simulations is not the one with the largest growth rate, which occurs for the wavelength about 1.0 cm, and could be accommodated by the computational box. Moreover, the growth rate of modes with the observed wavelength 2.0 cm, developing on the vertical profiles, is greater than the growth rate for the spanwise profiles. This is contrary to the observation that the spanwise oscillations precede the vertical oscillations and disagrees with the results of the similar analysis of Sabry *et al.* (1990). However, their analysis was performed using one-dimensional velocity profiles at the earlier location $X = 90$ cm where the profiles are less distorted than at the location $X = 98$ cm used in our work and consequently may result in different stability characteristics of the flow. Taken together, these results and controversies point to serious limitations of such a simplified stability analysis which depends on a somewhat arbitrary choice of characteristic velocity profiles. Nevertheless, with judicious choices some of the observed features of the flow instability can be predicted correctly.

Another simplified approach to the stability analysis of Görtler flow was proposed recently by Park & Huerre (1992). Assuming that the growth rate of the primary Görtler instability is much smaller than that of the instability produced by inflexional profiles, they use the flow field generated during an evolution of a two-dimensional Görtler flow as a basic flow and study its stability properties. Secondary instabilities of sinuous and varicose mode were discovered by integrating a linearized Navier–Stokes equations until a temporal trend $e^{(i\omega_r+\omega_i)t}$ is achieved, where ω_r is the phase speed and ω_i is the growth rate of the secondary instability. Their results show that both sinuous and varicose modes have much larger growth rates than the Görtler instability and the sinuous mode has a larger growth rate than the varicose mode. In our case the spanwise inflexional velocity profiles are responsible for the generation of sinuous modes and the vertical profiles are responsible for the generation of varicose modes. Thus the simulation results and our simplified stability analysis are broadly consistent with their conclusions.

3.4. *Secondary instabilities and structural features of the velocity field*

In the following discussion we decompose the total velocity field, denoted previously as $\boldsymbol{u}(x, y, z)$, in the following manner:

$$\boldsymbol{U}(x, y, z) = \boldsymbol{U}_b(z) + \boldsymbol{U}_g(y, z) + \boldsymbol{u}(x, y, z), \tag{25}$$

where

$$\boldsymbol{U}_b(z) = \frac{1}{L_x L_y} \int_0^{L_x} \int_0^{L_y} \boldsymbol{U}(x, y, z)\, dx\, dy, \tag{26}$$

$$\boldsymbol{U}_g(y, z) = \frac{1}{L_x} \int_0^{L_x} \boldsymbol{U}(x, y, z)\, dx - \boldsymbol{U}_b(z). \tag{27}$$

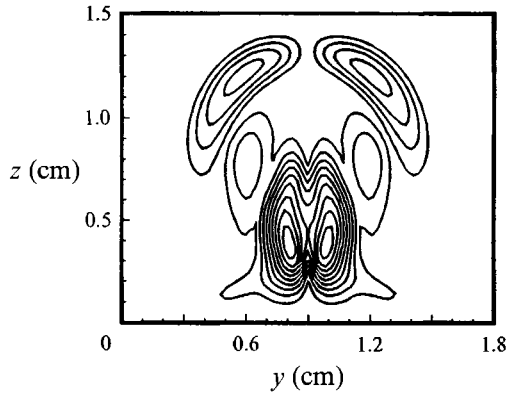

FIGURE 15. Iso-contours of the r.m.s. of the streamwise fluctuating velocity component $u_{\rm rms}/U_0$ in the (y,z)-plane at $X = 100$ cm in run B. Contour levels are $u_{\rm rms}/U_0 = 0.02, 0.04, \ldots$.

Here, $\boldsymbol{U}(x,y,z)$ is the total velocity, $\boldsymbol{U}_{\rm b}(z)$ is a basic flow which is the average of the total velocity taken over horizontal plane and is a function of the vertical coordinate z only, $\boldsymbol{U}_{\rm g}(y,z)$ is the Görtler velocity obtained as the average of the total velocity field taken over lines in the x-direction, with the basic flow $\boldsymbol{U}_{\rm b}$ subtracted, and $\boldsymbol{u}(x,y,z)$ signifies now only the fluctuating velocity component. Non-zero velocity $\boldsymbol{U}_{\rm g}(y,z)$ results from the primary Görtler instability of the base flow $\boldsymbol{U}_{\rm b}(z)$, and $\boldsymbol{u}(x,y,z)$ is the velocity perturbation resulting from the secondary instability of the two-dimensional Görtler flow $\boldsymbol{U}_{\rm b}+\boldsymbol{U}_{\rm g}$. We will use this decomposition and notation throughout the remainder of this paper. Similar definitions of averaged velocities were also used by Moser & Moin (1987) in their investigation of turbulent curved channel flow.

Note that for laminar Görtler flow the quantity $\boldsymbol{u}(x,y,z)$ vanishes and thus it can serve as a useful measure of the departure of the flow from a purely two-dimensional laminar state. Another indicator of the transition is the streamwise vorticity of the flow. In fully turbulent flows the r.m.s. values of the three fluctuating vorticity components are of the same order of magnitude. However, as pointed out by Blackwelder (1988), in laminar Görtler flow the streamwise vorticity component ω_x is much smaller than either the spanwise component ω_y or the vertical component ω_z. This is because the velocity components V and W that contribute to the streamwise vorticity are smaller than the streamwise velocity component U by a factor equal to Reynolds number (DiPrima & Stuart, 1972). Therefore a significant increase in the values of ω_x during the evolution of Görtler flow can serve as another useful measure of the departure of the flow from a purely laminar state. Both these measures were used in our work to identify the flow regions where secondary instabilities set in and the relation between these regions and the inflexional velocity profiles was investigated.

Figure 15 shows iso-contours of the r.m.s. values of the fluctuating streamwise velocity component:

$$u_{\rm rms}(y,z) = \left[\frac{1}{L_x}\int_0^{L_x} u^2(x,y,z)\,{\rm d}x\right]^{\frac{1}{2}}, \tag{28}$$

and figure 16 shows iso-contours of the streamwise vorticity component ω_x, both quantities obtained in run B and plotted in the (y,z)-plane at the streamwise location $X = 100$ cm. Results in figure 15 are in all essential aspects similar to the

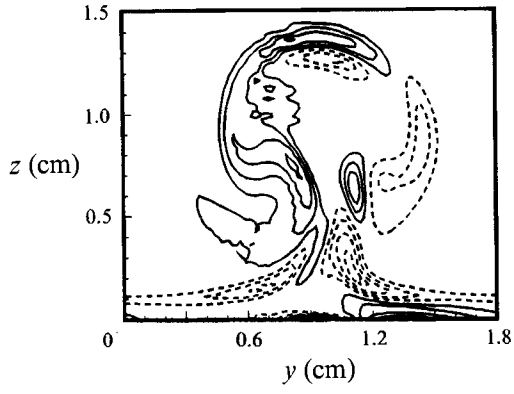

FIGURE 16. Iso-contours of the streamwise component of fluctuating vorticity ω_x in the (y, z)-plane at $X = 100$ cm in run B.

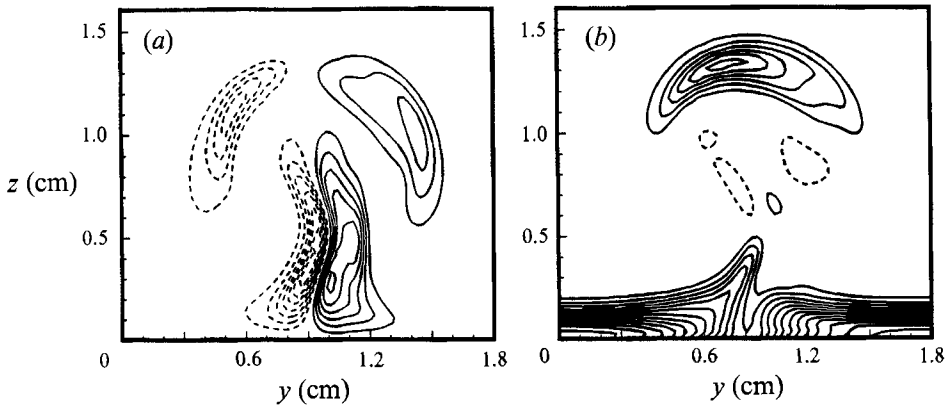

FIGURE 17. Iso-contours of gradients of the streamwise velocity component U in the (y, z)-plane at $X = 100$ cm in run B. Contours are normalized with the average of $(\partial U/\partial z)_w$ at the wall and their increment level is 0.1. (*a*) Iso-contours of shear $\partial U/\partial y$. (*b*) Iso-contours of shear $\partial U/\partial z$.

experimental results of Swearingen & Blackwelder (1987) for the same quantity, shown in figure 16 in their paper. Both $u_{\rm rms}$ and ω_x are characterized by the presence of the largest values in the stem of the 'mushroom' and smaller, local maxima on the sides of the 'mushroom's' hat. The vorticity also departs from zero in the region at the top of the 'mushroom's' hat.

In order to establish the relation between these quantities and the inflexional velocity profiles we computed and plotted the derivatives of the streamwise velocity U since the inflexion points are usually associated with the presence of strong spanwise and vertical shears of U. The instantaneous spanwise shear $\partial U/\partial y$, and the vertical shear $\partial U/\partial z$ are shown in figures 17(*a*) and 17(*b*), respectively. Shears are normalized by the average value of $\partial U/\partial z$ at the wall. Both quantities are again in close agreement with the experimental results of Swearingen & Blackwelder (1987) (see figure 18 in their paper). Examination of these results reveals that the large values of $u_{\rm rms}$ and ω_x correlate much better with the regions of large spanwise shear, $\partial U/\partial y$, than with the regions of large vertical shear, $\partial U/\partial z$. A particularly high level of correlation is observed between $u_{\rm rms}$ and $\partial U/\partial y$.

Customarily, regions of large vertical shear $\partial U/\partial z$ associated with the inflexional points on the vertical profiles of streamwise velocity are considered to be a primary

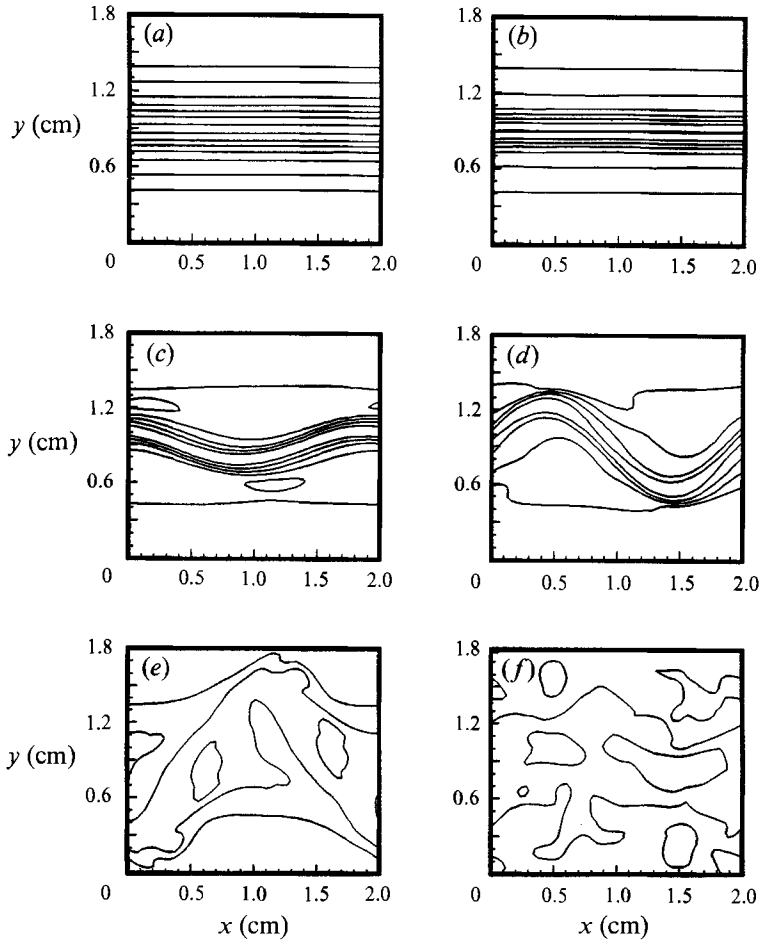

FIGURE 18. Iso-contours of the streamwise velocity U in the (x, y)-plane at $z/\delta \approx 0.4$, where $\delta \approx$ 1 cm, and six different streamwise locations from the leading edge: (*a*) $X = 89.8$ cm, (*b*) 94.0 cm, (*c*) 100.4 cm, (*d*) 102.5 cm, (*e*) 104.7 cm, (*f*) 115.3 cm (run B).

cause of the transition process. In our results, however, the region of large vertical shear away from the wall (figure 17*b*) does not correlate very well with the regions of large $u_{\rm rms}$, indicating that very little of the turbulent energy production is caused by it. It is nevertheless responsible for the appearance of the three-dimensional effects since its correlation with ω_x is significant. Therefore, our results indicate that in the transition process the regions of large spanwise shear $\partial U/\partial y$ may play a greater role than the regions of large vertical shear $\partial U/\partial z$. This conclusion is thus fully consistent with the experimental results of Swearingen & Blackwelder (1987) who showed a large degree of correlation between the regions of large spanwise shear and the regions of large streamwise velocity fluctuations. It appears that their work was the first investigation which systematically assessed the role of the spanwise and the vertical shears in the transition in wall-bounded flows and established the importance of the spanwise shear in this process.

Iso-contours of the streamwise velocity U in the (x, y)-plane for the initial phases of the transition and towards the end of run B, when the flow became more turbulent, are shown in figure 18. Associated iso-contours of the spanwise velocity V and the vertical velocity W in the (x, y)-plane are shown in figures 19 and 20, respectively.

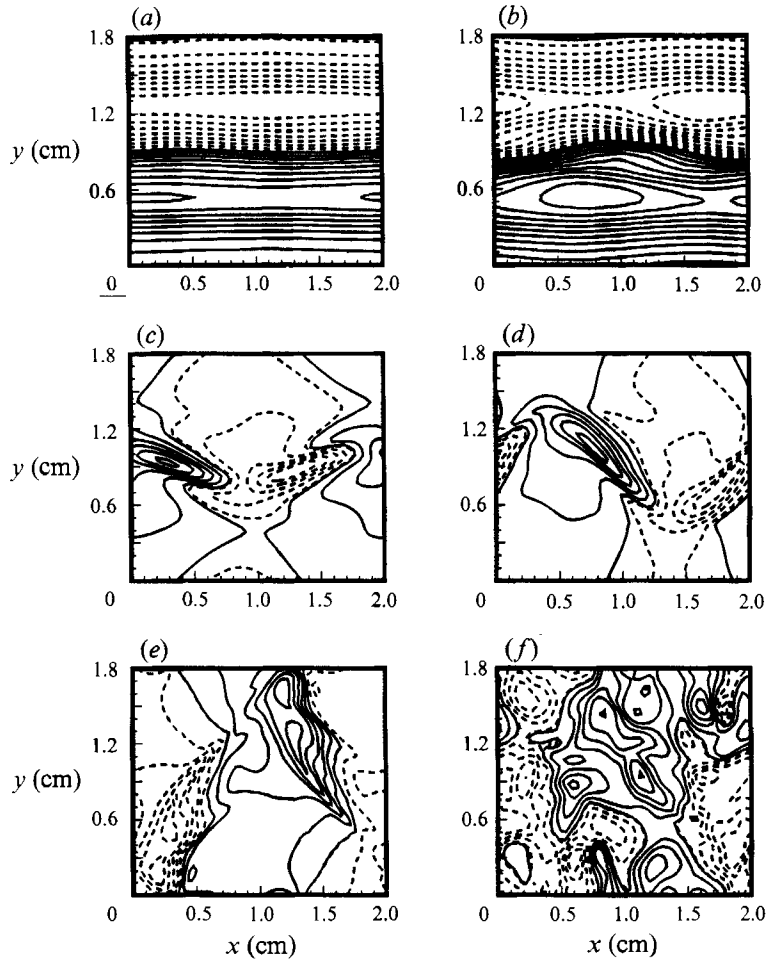

FIGURE 19. As figure 18 but for the spanwise velocity V.

The departure from a purely two-dimensional flow is marked by the appearance of spanwise oscillations with a wavelength equal to the streamwise extent of the computational domain. The oscillations start in the low-speed region at $z \approx 0.5\delta$, where the spanwise shear $\partial U/\partial y$ reaches values close to the maximum. This fact provides additional evidence of the importance of spanwise shear in the transition process.

By examining figure 20 we note that although only one wavelength of the perturbation is present in the computational domain, at several vertical locations z, two positive and two negative regions of the vertical velocity are seen while traversing the low-speed region ($y = 0.9$ cm) in the x-direction. However, while traversing the computational domain in the off-centre y-location one encounters only one positive and one negative region. Therefore, the frequencies of the W oscillations recorded by fixed probes at these two different spanwise locations will differ by a factor of two, with higher frequencies recorded in the low-speed region. This fact serves as the explanation of the difference between frequencies in the time series recorded in the simulations at different spanwise locations (§3.3). Such behaviour is typical for wake flows experiencing instabilities and was first observed by Kovasznay (1949) for a wake behind a cylinder.

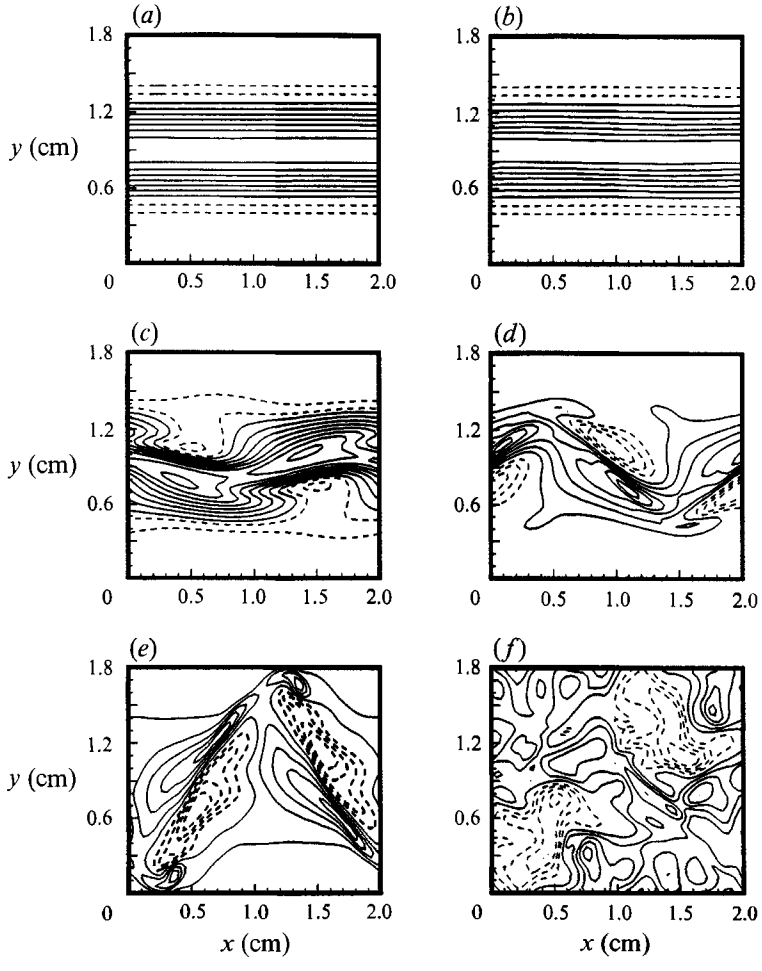

FIGURE 20. As figure 18 but for the vertical velocity W.

Associated iso-contours of the spanwise velocity V in the (x, z)-plane located in the low-speed region are shown in figure 21. In figure 22 iso-contours of the vertical velocity component W in the (x, z)-plane in the low-speed region for run B are presented. The oscillations in the vertical direction appear later than those in the spanwise direction. For instance, at the location $X = 89.8$ cm from the leading edge we do not observe any oscillations in the vertical direction even though the spanwise oscillations are already present (see figure 21). Periodic positive and negative regions of W, indicative of the oscillations in the vertical direction, appear at a larger distance from the leading edge, around $X = 100$ cm.

The two neighbouring regions of positive and negative values of W at $X = 102.5$ cm in figure 22 may be interpreted as a signature of a vortex aligned in the spanwise direction. It seems that it is possible to interpret such a vortex as a head of a hairpin vortex which is connected to the streamwise vortex pair on the sides of the 'mushroom' region. Indeed, it is seen in figure 16 that the streamwise vorticity ω_x has positive and negative peaks on both sides of the low-speed region at $z \approx 0.8\delta$. They could be attributed to the presence of the streamwise legs of the hairpin vortices. Figures 23(*a*) and 23(*b*) show the iso-surfaces of vorticity, with the

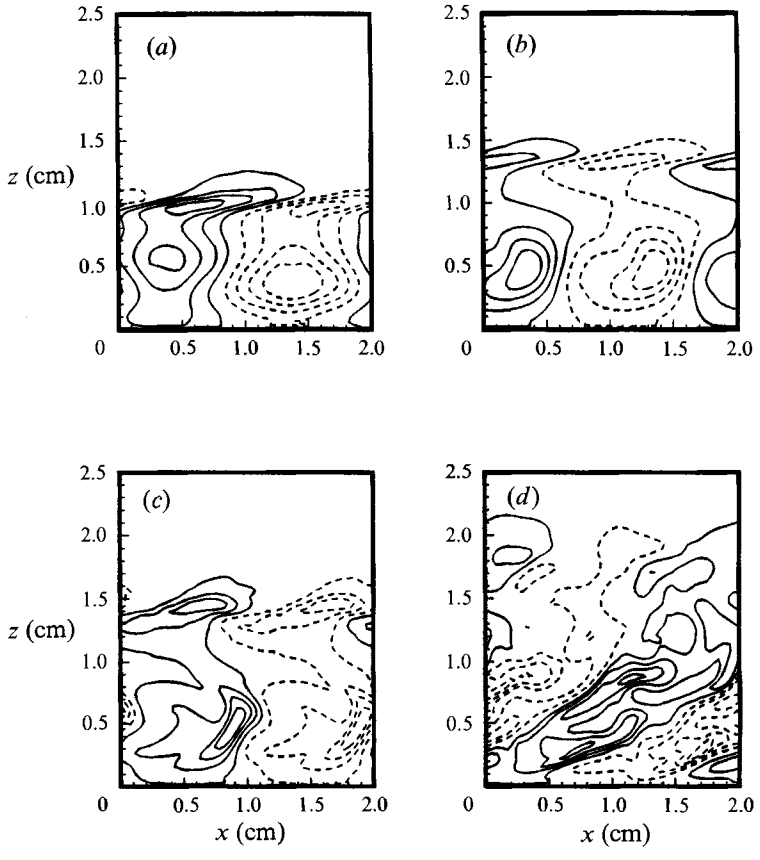

FIGURE 21. Iso-contours of the spanwise velocity V in the (x, z)-plane in the low-speed region at four different streamwise locations from the leading edge: (*a*) $X = 89.8$ cm, (*b*) 100.4 cm, (*c*) 102.5 cm, (*d*) 115.3 cm (run B).

contribution from the base flow $U_b(z)$ excluded, for runs A and B, respectively. In both cases a wavy region of concentrated vorticity in the low-speed region at the wall is observed. Away from the wall, the three dimensional vorticity structure exhibits very clearly a series of connected hairpin vortices in run A, though the vortices are less pronounced in run B. The spanwise vortices are associated with the varicose mode of the secondary instability and the high-vorticity structure at the wall is associated with the sinuous mode of the secondary instability.

3.5. *Kinetic energy balance analysis*

The kinetic energy balance analysis is often used in studying turbulence phenomena. Usually, in the kinetic energy balance analysis for turbulent boundary-layer flows (including flows over concave walls or in a curved channel) an assumption of statistical homogeneity in the horizontal planes is made and the mean flow is considered to be a function of z only as, for instance, in Moser & Moin (1987). However, because of the presence of the Görtler vortices in the flow considered here, the assumption of statistical homogeneity in the spanwise direction is clearly erroneous. Therefore, it may be very important to account explicitly for this inhomogeneity in the energy balance analysis if some important features of the energetics of the flow are not to be missed. For this reason we take here as the mean

flow the sum of the basic flow $U_b(z)$, which is the function of z only, and the Görtler vortical flow $U_g(y,z)$, which is the function of both y and z. Turbulent velocity is identified as the perturbation $\boldsymbol{u}(x,y,z)$ to this mean field and averages in the derivation of the kinetic energy balance equation are taken over lines in the x-direction, in which turbulent quantities are expected to be statistically homogeneous.

With this averaging procedure we use a standard method of deriving the kinetic energy balance equation (e.g. Monin & Yaglom 1971). Because of the wall curvature many 'extra' terms, which are not present in the corresponding equations for a flat-plate boundary layer, appear in the equation for Görtler flow. It has the following form in the curvilinear coordinate system used:

$$
\begin{aligned}
\frac{\partial \overline{q^2}}{\partial t} = {} & \left.\begin{aligned} & \Big[-\overline{uw}\Big(\frac{\partial U_b}{\partial z}+\frac{\kappa}{h}U_b\Big)-\overline{uw}\Big(\frac{\partial U_g}{\partial z}+\frac{\kappa}{h}U_g\Big) \\ & -\overline{uv}\frac{\partial U_g}{\partial y}-\overline{vw}\frac{\partial V_g}{\partial z}-\overline{vw}\frac{\partial W_g}{\partial y}\Big] \end{aligned}\right\} \text{production} \\
& +\Big[\frac{\kappa}{h}\overline{u^2}W_g-\overline{v^2}\frac{\partial V_g}{\partial y}-\overline{w^2}\frac{\partial W_g}{\partial z}\Big] && \text{convection} \\
& +\Big[\frac{\kappa}{h}\overline{W'q^2}-\frac{\partial \overline{W'q^2}}{\partial z}-\frac{\partial \overline{V'q^2}}{\partial y}\Big] && \text{turbulent diffusion} \\
& -\frac{1}{\rho}\Big[\overline{\frac{u}{h}\frac{\partial p}{\partial x}+v\frac{\partial p}{\partial y}+w\frac{\partial p}{\partial z}}\Big] && \text{pressure redistribution} \\
& +\nu\Big[\frac{\partial^2 \overline{q^2}}{\partial z^2}+\frac{\partial^2 \overline{q^2}}{\partial y^2}-\frac{\kappa}{h}\frac{\partial \overline{q^2}}{\partial z}\Big] && \text{viscous diffusion} \\
& -\nu\Big[\overline{\Big(\frac{1}{h}\frac{\partial u}{\partial x}-\frac{\kappa}{h}w\Big)^2}+\overline{\Big(\frac{\partial u}{\partial y}\Big)^2}+\overline{\Big(\frac{\partial u}{\partial z}\Big)^2} \\
& +\frac{1}{h^2}\overline{\Big(\frac{\partial v}{\partial x}\Big)^2}+\overline{\Big(\frac{\partial v}{\partial y}\Big)^2}+\overline{\Big(\frac{\partial v}{\partial z}\Big)^2} && \text{dissipation} \\
& +\overline{\Big(\frac{1}{h}\frac{\partial w}{\partial x}+\frac{\kappa}{h}u\Big)^2}+\overline{\Big(\frac{\partial w}{\partial y}\Big)^2}+\overline{\Big(\frac{\partial w}{\partial z}\Big)^2}\Big],
\end{aligned}
\tag{29}
$$

where $q^2=\frac{1}{2}(u^2+v^2+w^2)$ is the perturbation energy, $h=1-\kappa z$, and the overbar denotes averaging over lines in the x-direction. The terms on the right-hand side of (29) are functions of the variables y and z.

We are interested mostly in identifying the turbulent energy production mechanisms in the transition process and our analysis will concentrate on the production term which describes how the perturbation energy is produced by Reynolds stresses working against the basic flow and the Görtler vortical flow. The production term consists of five sub-terms, each describing the contributions that various components of the mean shear make to the turbulent energy production. Figures 24(a) and 24(b) show iso-contour plots of $-\overline{uw}(\partial U_b/\partial z+(\kappa/h)U_b)$ and $-\overline{uw}(\partial U_g/\partial z+(\kappa/h)U_g)$, respectively, for run B at $X=98$ cm. Both these terms describe the turbulent energy production caused by instabilities of the vertical velocity profiles of the basic flow $U_b(z)$ and the Görtler component $U_g(y,z)$, respectively. This mechanism is most effective away from the wall, on the sides of the

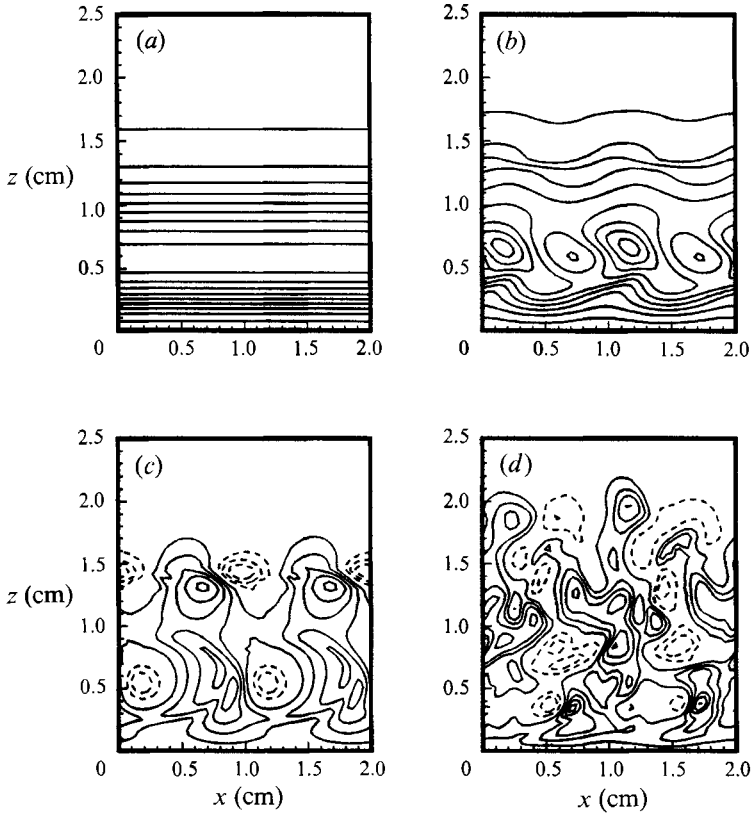

FIGURE 22. As figure 21 but for the vertical velocity W.

'mushroom' structure, and is apparently associated with the varicose mode of the secondary instability. Both these terms are of the same order of magnitude, and when integrated over the whole plane, they make comparable contributions to the overall energy production. The term $-\overline{uv}\,\partial U_g/\partial y$ is plotted in figure 24(*c*). It describes the energy production caused by instabilities of the spanwise velocity profiles and its maximum value is greater by the factor 20 than the maxima in the two previous plots. Its integral contribution to the total energy production is one order of magnitude greater than combined contributions of all remaining terms. The production mechanism described by this important term is most effective in the low-speed region, at the distance $z \approx 0.5\delta$ from the wall, where the largest spanwise shear is present and where the sinuous mode of the secondary instability originates. Indeed, in figure 24(*c*) the regions of large production correlate very well with the regions of large spanwise shear (figure 17*a*), and similarly, in figures 24(*a*) and 24(*b*) the production terms correlate well with the regions of large vertical shears (figure 17*b*). The two remaining turbulent energy production terms, associated with the gradients of the spanwise, V_g, and the normal, W_g, Görtler velocity components were found to contribute negligibly to the production (Liu 1991) and are not discussed here.

The major conclusion from the analysis of the turbulent energy production term for the Görtler flow is that the dominant energy production mechanisms in the transition process are instabilities of the wake-like shear layer located in the upwash

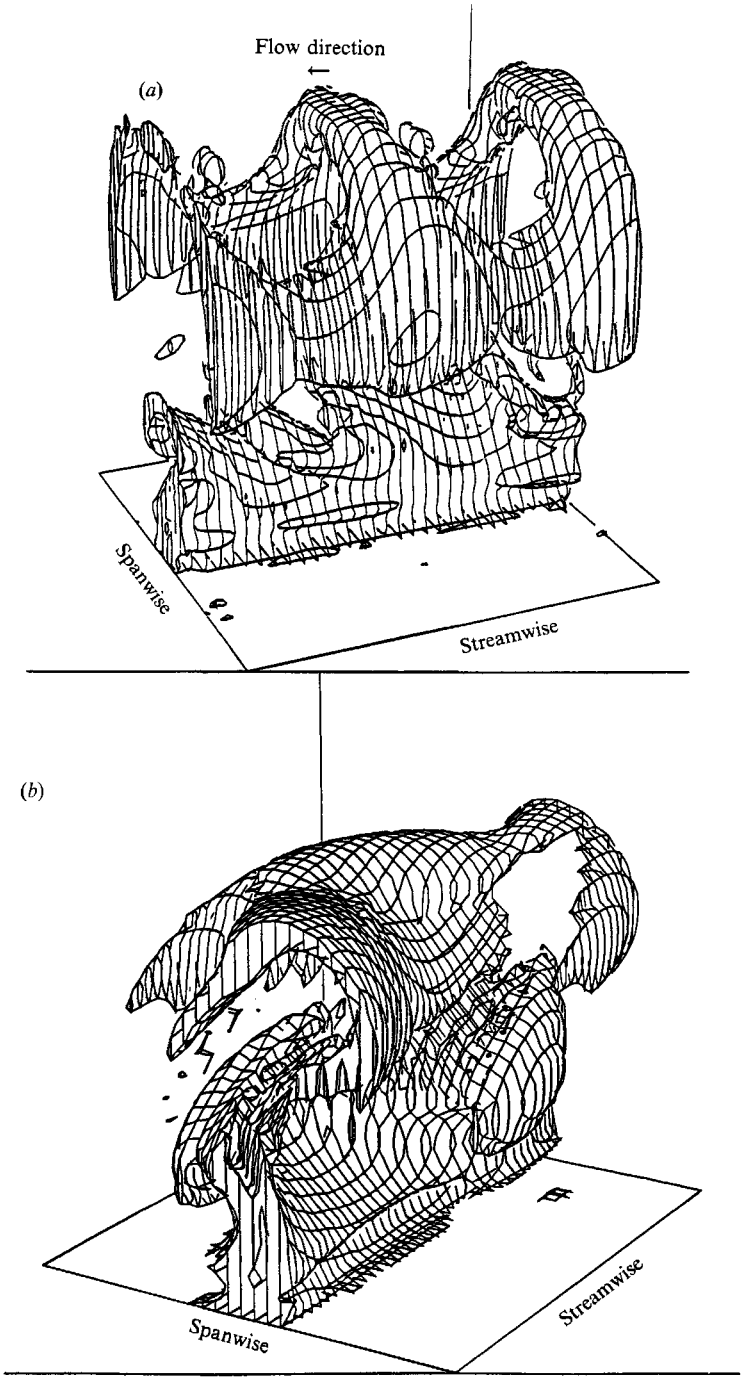

FIGURE 23. Iso-surfaces of vorticity computed from the perturbation velocity $\boldsymbol{U}_g(y,z)+\boldsymbol{u}(x,y,z)$; (*a*) run A, (*b*) run B.

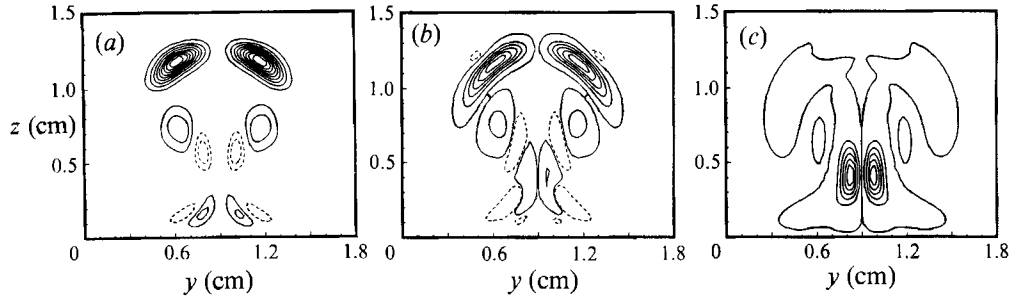

FIGURE 24. Iso-contour plots of the turbulent energy production terms in the (y,z)-plane at the streamwise location $X = 98$ cm in run B. All quantities normalized by $\overline{u_\tau^4}/\nu$, where ν is the kinematic viscosity and $\overline{u_\tau^4}$ is the average over the wall of the fourth power of the friction velocity, $u_\tau = (\nu(\partial U/\partial z)_w)^{\frac{1}{2}}$. (*a*) $-\overline{uw}(\partial U_b/\partial z + (\kappa/h)U_b)$; the maximum value in this figure is 0.477×10^{-5}. (*b*) $-\overline{uw}(\partial U_g/\partial z + (\kappa/h)U_g)$; the maximum value in this figure is 0.674×10^{-5}. (*c*) $\overline{uv}\,\partial U_g/\partial y$; the maximum value in this figure is 0.126×10^{-3}.

region between the vortices. This result provides additional evidence supporting the assertion that spanwise shear plays a more important role in the initial phases of the transition process than vertical shear.

It should be noted that the importance of spanwise shear in turbulent energy production could not be easily established if the customary averaging over horizontal planes were used in deriving the kinetic energy balance equation. With such an averaging procedure the sum $\boldsymbol{u}'(x,y,z) = \boldsymbol{U}_g(y,z) + \boldsymbol{u}(x,y,z)$ is treated as a fluctuating velocity and $\boldsymbol{U}_b(z)$ is a basic flow, resulting in the following form of the energy production term:

$$-\overline{u'w'}\left(\frac{\partial U_b}{\partial z} + \frac{\kappa}{h}U_b\right), \tag{30}$$

with no dependence on the spanwise direction y. It may be expected that similar difficulties will be encountered in describing any turbulent flow which contains long-lived coherent structures. Including the velocity associated with the coherent structures into the definition of the fluctuating turbulent velocity may obscure some important physics of the flow.

3.6. *Weakly turbulent regime*

In figure 5, at the end of run B, the average boundary-layer displacement thickness and the average vertical gradient of the streamwise velocity measured in the low-speed region and in the high-speed region approach the same values, which is indicative of the flow becoming weakly turbulent.

Figure 25 shows iso-contours of the total streamwise velocity and r.m.s. values of the turbulent streamwise velocity component in the (y,z)-plane at the end of run B. These, as well as all other physical quantities we investigated, have their maxima near the wall. Therefore, this region located within distance 0.25δ from the wall seems to be responsible for most of the subsequent turbulence production. Also, in the final stages of the simulations, distinctive S-shaped inflexional velocity profiles and the associated local vertical and horizontal shear layers are destroyed by turbulence, thereby losing capability to cause further instabilities.

It is interesting to note in figure 25(*a*) that the streamwise velocity shows two small 'mushroom' structures near the wall, one in the original low-speed region and the other one in the original high-speed region. Similar structures can also be found

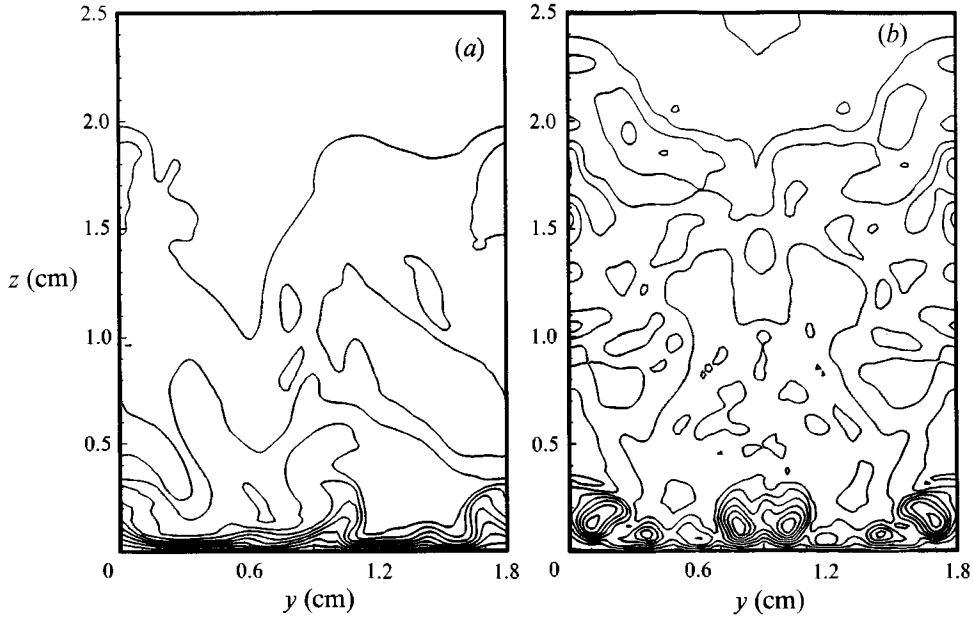

FIGURE 25. Iso-contours in the (y, z)-plane at $X = 113$ cm in run B: (*a*) the streamwise velocity component U, (*b*) the r.m.s. of the streamwise fluctuating velocity component u_{rms}.

in figure 25(*b*). One may speculate that additional flow instabilities in the vicinity of the wall in the turbulent regime are responsible for the generation of these structures. However, we have not investigated the turbulent regime further.

4. Conclusions

Investigations of counter-rotating vortices occurring in Görtler flow are very helpful in understanding the dynamics of similar vortices encountered in transitional and turbulent wall-bounded flows. A numerical code to simulate Görtler flow has been developed and it was demonstrated that the code can accurately predict the linear growth rates of the primary Görtler vortices and is capable of generating the Görtler vortices naturally from the background noise. The direct numerical simulations results for the evolution of three-dimensional Görtler flow are in a good qualitative and quantitative agreement with a number of experimental results. Inflexional velocity profiles of the streamwise velocity, generated by the action of the counter-rotating vortices, are found in the simulations both in the spanwise and in the vertical directions. A standard stability analysis performed for such one-dimensional velocity profiles indicates that their secondary instabilities are the main mechanism of the transition to turbulence in such flows. The numerical results convincingly show that the spanwise inflexional profile and the associated shear $\partial U/\partial y$ play a more important role in the transition process than the vertical inflexional profile and the shear $\partial U/\partial z$, which are conventionally considered the main cause of the transition. After the transition process begins, velocity oscillations in the spanwise and vertical directions with distinct frequencies can be observed in the simulations. The spanwise oscillations appear first and are associated with a sinuous motion of the unstable low-speed streaks. The vertical oscillations are observed later than the spanwise oscillations and are associated with the appearance of a varicose

mode of the secondary instability in the form of hairpin vortices. Close to the transition point a three-dimensional vorticity structure suggests a series of such connected hairpin vortices in the outer regions of the boundary layer. However, in the transition process these hairpin vortices play an apparently smaller role than the streamwise vortical structure which develops in the vicinity of the wall in the low-speed region between the Görtler vortices. The analysis of the kinetic energy balance equation, which takes into account spanwise inhomogeneity of the mean flow, shows that the production term arising from the spanwise shear induced by the Görtler vortices is much larger than the production terms arising from the interaction of turbulence with the vertical shear, reinforcing conclusions about the importance of the spanwise variations of the flow on the transition process. At the end of simulations we find that almost all physical quantities have maximum values near the wall.

The authors benefitted from numerous discussions with R. F. Blackwelder. S. A. Orszag kindly agreed to our using the numerical code FLOGUN in our work. This work was supported by the US Office of Naval Research under URIP Contract No. N00014-86-0679 and by the Research Initiation Grant from the Powell Foundation. Computer time was provided by the San Diego Supercomputer Center.

REFERENCES

ACARLAR, M. S. & SMITH, C. R. 1987*a* A study of hairpin vortices in a laminar boundary layer. Part 1. Hairpin vortices generated by a hemisphere protuberance. *J. Fluid Mech.* **175**, 1–41.

ACARLAR, M. S. & SMITH, C. R. 1987*b* A study of hairpin vortices in a laminar boundary layer. Part 2. Hairpin vortices generated by fluid injection. *J. Fluid Mech.* **175**, 43–83.

BIPPES, H. 1972 Experimentelle Untersuchung des Laminar Turbulenten Umschlages an einer Parallel Angestromten Konkaven Wand. *Heidel. Akad. Wiss., Naturwiss. Kl., Sitzungsber.* **3**, 103–180.

BLACKWELDER, R. F. 1983 Analogies between transitional and turbulent boundary layers. *Phys. Fluids* **26**, 2807–2815.

BLACKWELDER, R. F. 1988 Coherent structures associated with turbulent transport. In *Transport Phenomena in Turbulent Flow* (ed. M. Hirata & N. Kasagi), p. 69. Hemisphere.

CANUTO, C., HUSSAINI, M. Y., QUARTERONI, A. & ZANG, T. A. 1988 *Spectral Methods in Fluid Dynamics*. Springer.

DIPRIMA, R. C. & STUART, J. T. 1972 Non-local effects in the stability of flow between concentric rotating cylinders. *J. Fluid Mech.* **54**, 393–415.

FLORYAN, J. M. 1991 On the Görtler instability of boundary layers. *Prog. Aerospace Sci.* **28**, 235–271.

FLORYAN, J. M. & SARIC, W. S. 1979 Stability of Görtler vortices in boundary layers. *AIAA J.* **20**, 316–324.

FORTIN, M., PEYRET, R. & TEMAM, R. 1971 Resolution numerique des equations de Navier–Stokes pour un fluide incompressible. *J. Méc.* **10**, 357–390.

GÖRTLER, H. 1940 Über eine Dreidimensionale Instabilität Laminarer Grenzshichten an Konkaven Wänden. *Nachr. Wiss. Ges. Göttingen Math. Phys. Kl.* **2**, 1–26.

GOTTLIEB, D., HUSSAINI, M. Y. & ORSZAG, S. A. 1984 Theory and Application of Spectral Methods. In *Spectral Methods for Partial Differential Equations*. SIAM.

HALL, P. 1982 Taylor–Görtler vortices in fully developed boundary layer flows: linear theory. *J. Fluid Mech.* **124**, 475–494.

HALL, P. 1983 The linear development of Görtler vortices in growing boundary layer. *J. Fluid Mech.* **130**, 41–58.

HALL, P. 1988 The nonlinear development of Görtler vortices in growing boundary layers. *J. Fluid Mech.* **193**, 243–266.

HALL, P. & HORSEMAN, N. J. 1991 The linear inviscid secondary instability of longitudinal vortex structures in boundary layers. *J. Fluid Mech.* **232**, 357–375.

HÄMMERLIN, G. 1955 Über das Eigenwertproblem der Dreidimensionalen Instabilität Laminarer Grenzschichten an Konkaven Wänden. *J. Rat. Mech. Anal.* **4**, 279–321.

HERBERT, T. 1976 On stability of the boundary layer along a concave wall. *Arch. Mech.* **28**, 1039–1055.

KLINE, S. J. & ROBINSON, S. K. 1989 Turbulent boundary layer structure: progress, status, and challenges. In *Proc. 2nd IUTAM Symp. Struct. of Turbul. and Drag Reduct., Zurich* (ed. A. Gyr). Springer.

KOVASZNAY, L. S. G. 1949 Hot-wire investigation of the wake behind cylinders at low Reynolds numbers. *Proc. R. Soc. Lond.* A **198**, 174–190.

LIEPMANN, H. W. 1945 Investigation of boundary layer transition on concave walls. *NACA Wartime Rep.* W87.

LIU, W. 1991 Direct numerical simulation of transition to turbulence in Görtler flow. Ph.D. thesis, University of Southern California, Los Angeles.

MONIN, A. S. & YAGLOM, A. M. 1971 *Statistical Fluid Mechanics: Mechanics of Turbulence*, Vol. I, pp. 373–388. The MIT Press.

MOSER, R. D. & MOIN, P. 1987 The effects of curvature in wall-bounded turbulent flows. *J. Fluid Mech.* **175**, 479–510.

ORSZAG, S. A. & KELLS, L. C. 1980 Transition to turbulence in plane Poiseuille flow and plane Couette flow. *J. Fluid Mech.* **96**, 159–205.

PARK, D. S. & HUERRE, P. 1992 Görtler vortex growth and breakdown. *J. Fluid Mech.* (submitted).

PEERHOSSAINI, H. & WESFRIED, J. E. 1988 On the inner structure of streamwise Görtler vortices. *Intl J. Heat Fluid Flow* **9**, 12–18.

ROBINSON, S. K. 1991 Coherent motions in the turbulent boundary layer. *Ann. Rev. Fluid Mech.* **23**, 601–639.

SABRY, A. S. & LIU, J. T. C. 1988 Nonlinear development of Görtler vortices and the generation of high shear layers in the boundary layers. In *Proc. Symp. in Honor of C. C. Lin* (ed. D. J. Benney, F. H. Shu & C. Yuan). World Scientific.

SABRY, A. S. & LIU, J. T. C. 1991 Longitudinal vorticity elements in boundary layers: nonlinear development from initial Görtler vortices as a prototype problem. *J. Fluid Mech.* **231**, 615–663.

SABRY, A. S., YU, X. & LIU, J. T. C. 1990 Secondary instabilities of three-dimensional inflectional velocity profiles resulting from longitudinal vorticity elements in boundary layers. In *Proc. 3rd IUTAM Symp. Laminar-Turbulent Trans.* (ed. D. Arnal & R. Michel), pp. 441–451. Springer.

SMITH, A. M. 1955 On the growth of Taylor–Görtler vortices along highly concave walls. *Q. J. Appl. Maths* **13**, 233–262.

SWEARINGEN, J. D. & BLACKWELDER, R. F. 1987 The growth and breakdown of streamwise vortices in the presence of a wall. *J. Fluid Mech.* **182**, 255–290.

TANI, I. 1962 Production of longitudinal vortices in the boundary layer along a concave wall. *J. Geophys. Res.* **67**, 3075–3080.

TANI, I. & AIHARA, Y. 1969 Görtler vortices and boundary-layer transition. *Z. Angew. Math. Phys.* **20**, 609–618.

WINOTO, S. H. & CRANE, R. I. 1980 Vortex structure in laminar boundary layers on a concave walls. *Intl J. Heat Fluid Flow* **2**, 221–231.

WORTMANN, F. X. 1969 Visualization of transition. *J. Fluid Mech.* **38**, 473–480.

YU, X. & LIU, J. T. C. 1991 The secondary instability in Görtler flow. *Phys. Fluids* A **3**, 1845–1847.

ZANG, T. & HUSSAINI, M. Y. 1986 On spectral multigrid methods for the time-dependent Navier–Stokes equation. *Appl. Math. Comput.* **19**, 359–372.